



On the role of climate modes in modulating the air-sea CO₂ fluxes in Eastern Boundary Upwelling Systems

Riley X. Brady¹, Nicole S. Lovenduski¹, Michael A. Alexander², Michael Jacox^{2,3}, and Nicolas Gruber⁴

¹Department of Atmospheric and Oceanic Sciences and Institute of Arctic and Alpine Research, University of Colorado, Boulder, CO, USA

²NOAA/ESRL, Boulder, CO, USA

³NOAA/SWFSC, Monterey, CA, USA

⁴Environmental Physics, Institute of Biogeochemistry and Pollutant Dynamics, ETH Zürich, Zürich, Switzerland

Correspondence: Riley X. Brady (riley.brady@colorado.edu)

Abstract. The air-sea CO₂ fluxes in Eastern Boundary Upwelling Systems (EBUS) vary strongly in time and space with some of the highest flux densities globally. The processes controlling this variability have not yet been investigated consistently across all four major EBUS, i.e., the California (CalCS), Humboldt (HumCS), Canary (CanCS), and Benguela (BenCS) Current Systems. In this study, we diagnose the physical and biological mechanisms that contribute to historical (1920-2015) CO₂ flux variability in these regions using simulation results from the Community Earth System Model Large Ensemble (CESM-LENS), a global coupled climate model ensemble that is forced by historical and RCP8.5 radiative forcing. Differences between simulations can be attributed entirely to internal climate variability. We find that the deviations from the ensemble mean, i.e., the anomalous CO₂ fluxes, in the CalCS and CanCS are strongly affected by modes of variability associated with atmospheric subtropical gyres: the North Pacific Gyre Oscillation (NPGO) and the North Atlantic Oscillation (NAO), respectively. The CalCS (CanCS) has anomalous uptake (outgassing) of CO₂ during the positive phase of the NPGO (NAO). The HumCS is mainly affected by El Niño Southern Oscillation (ENSO), with anomalous uptake of CO₂ during an El Niño event. Variations in dissolved inorganic carbon (DIC) and sea surface temperature (SST) are the major contributors to these anomalous CO₂ fluxes, and are generally driven by changes to gyre circulation, upwelling, the mixed layer depth, and biological processes. A better understanding of the sensitivity of EBUS CO₂ fluxes to modes of climate variability may improve our ability to predict the ocean–atmosphere carbon cycle in EBUS, which are particularly susceptible to ocean acidification.

1 Introduction

The four major Eastern Boundary Upwelling Systems (EBUS) occur at the eastern edges of subtropical gyres in the Atlantic and Pacific oceans – the California (CalCS), Humboldt (HumCS), Canary (CanCS), and Benguela (BenCS) Current Systems. These regions are characterized by seasonal or permanent equatorward winds that cause upwelling due to both offshore Ekman transport as well as wind stress curl-driven Ekman suction within the first 200 km of the coastline (Chavez and Messié, 2009). Upwelling delivers deep waters with respired nutrients to the surface, fueling primary production and ultimately supporting fisheries that are highly productive with respect to the small surface area they cover (Ryther, 1969). Upwelled waters also



have an elevated dissolved inorganic carbon (DIC) content, which enhances the partial pressure of carbon dioxide ($p\text{CO}_2$) and reduces the pH and carbonate ion concentration. The carbonate chemistry of EBUS is controlled by a complex interplay of physical and biological processes: entrainment of subsurface waters, horizontal advection, upwelling and vertical mixing, temperature changes, photosynthesis, respiration, and calcium carbonate formation and dissolution (DeGrandpre et al., 1998; King et al., 2007). These terms combine to dictate oceanic $p\text{CO}_2$, which drives the $p\text{CO}_2$ gradient between the ocean and atmosphere ($\Delta p\text{CO}_2$), thus contributing to the magnitude and determining the direction of air-sea CO_2 fluxes.

Although coastal oceans around the world have a small net contribution to the global air-sea CO_2 flux, they are characterized by a high CO_2 flux density, or magnitude of air-sea CO_2 exchange per unit area (Laruelle et al., 2010, 2014; Gruber, 2015; Laruelle et al., 2017). Low-latitude upwelling systems, such as the HumCS and CanCS, tend to be net outgassing systems, due to their relatively warm waters and persistent upwelling, which are not fully compensated for by enhanced biological productivity. Because of their colder temperatures and more efficient biology, mid-latitude systems, such as the CalCS and BenCS, act as weak CO_2 sinks that can become CO_2 sources during certain seasons (Borges and Frankignoulle, 2002; Hales et al., 2005; Cai et al., 2006; Gregor and Monteiro, 2013). Surface ocean $p\text{CO}_2$ and thus air-sea CO_2 flux in EBUS exhibits high temporal variability at sub-seasonal, seasonal, and interannual time scales (Friederich et al., 2002; González-Dávila et al., 2009; Leinweber et al., 2009; Evans et al., 2011; Turi et al., 2014). While the pronounced temporal variability of CO_2 fluxes in EBUS has been documented by numerous studies, little work has been done to associate it directly with internal climate variability (variability arising from unforced interactions between components of the climate system).

As coastal systems provide the majority of marine resources harvested by humans (Pauly and Christensen, 1995) and CO_2 fluxes are notoriously difficult to measure, studies have instead focused on associating major modes of climate variability with variability in the physics and biology of EBUS (e.g., Barber and Chavez, 1983; Chavez et al., 2002). However, internal variability in EBUS CO_2 fluxes is important to study, as it imposes variability on the fractional uptake of anthropogenic carbon by the ocean as well as modifies the surface ocean pH, potentially leading to intermittent ocean acidification events in the future (Kwiatkowski and Orr, 2018; Landschützer et al., 2018). Previous studies have tended to analyze the influence of internal climate variability on CO_2 fluxes for a single EBUS and a single climate event. El Niño Southern Oscillation (ENSO) has been observed to drive anomalous CO_2 flux in both the CalCS (Friederich et al., 2002) and HumCS (Chavez et al., 1999). El Niño (La Niña) tends to cause uptake (outgassing) anomalies in these systems, primarily through modifications to the thermocline depth and upwelling rates of nutrient- and carbon-rich waters, which in turn alters biological activity. However, upwelling-favorable winds can persist during some El Niños in the HumCS (Huyer et al., 1987), leading to persistent or enhanced outgassing of CO_2 to the atmosphere (Torres et al., 2003). Longer-term fluctuations in the CalCS arise from Pacific Decadal Variability. Although studies have linked the Pacific Decadal Oscillation (PDO) and North Pacific Gyre Oscillation (NPGO) to low frequency changes in upwelling rates, nutrient fluxes, and fisheries in the CalCS (e.g., Chenillat et al., 2012; Chhak and Di Lorenzo, 2007; Di Lorenzo et al., 2008; Mantua et al., 1997), no work has been done to directly investigate the effect of decadal variability on Pacific EBUS CO_2 fluxes in particular. However, studies have shown that a positive PDO intensifies the trade winds along the equatorial Pacific, leading to intensified upwelling and thus outgassing (Feely et al., 2006; Takahashi et al., 2003). The response of HumCS CO_2 fluxes to the PDO might be similar. To the best of our knowledge, there



have been no studies exploring CO₂ flux sensitivity to large modes of climate variability in the two Atlantic EBUS. However, Cropper et al. (2014) found that the North Atlantic Oscillation (NAO) plays a major role in modulating interannual variability of coastal upwelling in the CanCS and Borges et al. (2003) link the NAO to decadal variability in sardine catch. Variability in upwelling and biology in the BenCS has been linked to Benguela Niños (Shannon et al., 1986), ENSO teleconnections, and the Southern Annular Mode (Reason et al., 2006; Hutchings et al., 2009). However, decadal-scale oscillations like the NAO or PDO do not appear to be present in the South Atlantic (Hutchings et al., 2009). In summary, prior research has illuminated the large temporal variability of *p*CO₂ and CO₂ fluxes in EBUS and few have analyzed the impacts of single climate events on anomalous CO₂ fluxes in the CalCS and HumCS. Past studies tend to focus instead on linking internal climate variability to upwelling, nutrients, and fish catch. Our study aims to address this gap by identifying the major mode of climate variability associated with anomalous CO₂ fluxes in the major EBUS and by further investigating the dynamics that underpin these anomalies.

Previous studies have utilized observations (*e.g.*, Boyd et al., 1987; Friederich et al., 2002; Chavez et al., 2002; Santana-Casiano et al., 2007; Di Lorenzo et al., 2008, 2009) and high-resolution hindcast simulations (Jacox et al., 2015; Frischknecht et al., 2015; Turi et al., 2017; Mogollón and Calil, 2017) to explore the relationship between climate variability and EBUS biogeochemistry, such as dissolved oxygen, pH, nitrate supply, and primary production. Direct observation is of course the most desirable tool for understanding the real world, but it is not feasible for this study due to the sparsity of *p*CO₂ and CO₂ flux measurements and the relatively short length of observational time series. Regional hindcast simulations are beneficial for two main reasons. First, they tend to have a higher resolution than the standard 1° x 1° resolution of global Earth System Models (ESMs) and thus explicitly resolve the coastal upwelling process. Second, the ocean model component is generally forced by an atmospheric reanalysis product so that the model more closely resembles reality than a freely coupled ESM. However, single realizations provide a limited sample size of internal variability and confound the impacts of external forcing (*e.g.*, land use change, fossil fuel emissions, volcanic eruptions) with internal climate variability. The former is problematic, because ENSO events evolve differently in the tropics (Capotondi et al., 2015) and mid-latitude atmospheric noise can obscure the tropical-extratropical connections associated with climate modes such as ENSO, causing a diversity of responses in EBUS (Deser et al., 2017, 2018). The latter makes it difficult to isolate the internal component of variability in CO₂ fluxes from the seasonal cycle and anthropogenic and other external forcing. One solution to this problem is to use a single-model ensemble that is derived by introducing perturbations to the initial state of the climate system. This gives rise to a set of realizations with unique representations of internal climate variability and gives one access to many hundred ENSO events. By performing historical experiments with increasing atmospheric CO₂ rather than a long control simulation, we can account for variability in air-sea flux of both natural CO₂ (the component of ocean CO₂ in equilibrium with pre-industrial atmospheric CO₂) and anthropogenic CO₂.

In this study, we utilize output from the single-model Community Earth System Model “Large Ensemble” (CESM-LENS; Kay et al., 2015; Lovenduski et al., 2016) to identify major modes of climate variability that are associated with anomalous CO₂ fluxes in the major EBUS. We expand on this by investigating the physical and biological drivers that underpin these anomalies. The single-model ensemble allows for an assessment of both the forced signal and the CO₂ flux response to internal



climate variability. Since the simulations are forced with historical CO₂ emissions, each member accounts for variability in both natural and anthropogenic CO₂. Furthermore, the availability of 34 simulations allows us to find statistically robust relationships between anomalous CO₂ fluxes and internal climate variability.

2 Methods

5 2.1 Model Configuration

We utilize monthly mean output from 34 members of the CESM-LENS (Kay et al., 2015; Lovenduski et al., 2016), which is derived from the Community Earth System Model, version 1, with the Community Atmosphere Model, version 5 (CESM1(CAM5); Hurrell et al., 2013). Along with standard atmosphere, ocean, land, and sea ice components, the CESM-LENS simulations include land and ocean biogeochemistry. The ocean biogeochemical component of CESM1(CAM5) is the Biogeochemical
10 Elemental Cycling (BEC) model, which has three phytoplankton functional groups and tracks the cycling of C, N, P, Fe, Si, and O in the ocean. Further information on the implementation of BEC in CESM1 can be found in Moore et al. (2013) and Lindsay et al. (2014). The ocean component is the Parallel Ocean Program, version 2 (Smith et al., 2010) and has a nominal 1° horizontal resolution with vertical resolution of 10 m through the upper 250 m, thereby resolving the Ekman layer. Due to the coarse horizontal resolution, neither curl-driven nor coastal upwelling is directly resolved, but both are represented in the
15 model. A more detailed discussion of coastal upwelling in the CESM-LENS for the CalCS in particular can be found in (Brady et al., 2017).

The 34 ensemble members of CESM-LENS were generated using round-off level (order 10⁻¹⁴ K) level perturbations in the initial atmospheric temperature. (Kay et al., 2015). This generates an ensemble of simulations that diverge solely due to the influence of internal variability. Each ensemble member was forced with a common external forcing: historical radiative
20 forcing from 1920 to 2005 and RCP8.5 radiative forcing from 2006 to 2100. In contrast to a pre-industrial control simulation, CESM-LENS includes the addition of anthropogenic carbon to air-sea CO₂ fluxes. Anthropogenic CO₂ is explicitly separated from natural CO₂ by computing air-sea CO₂ fluxes relative to a constant 284.7 ppm pre-industrial atmosphere and subtracting it from CO₂ fluxes responding to the evolving atmosphere under historical and RCP8.5 radiative forcing.

2.2 Upwelling Regions

25 Upwelling regions in each EBUS span approximately the 10° latitude of most active upwelling as defined by Chavez and Messié (2009); we shifted the CanCS upwelling domain north by 9° to capture the more intense upwelling off the Western Sahara in CESM1 (Table 1). Following Turi et al. (2014), the EBUS upwelling regions span from the coastline to 800 km offshore. The black outlines in Figure 1e–h display these regions. The CESM-LENS ensemble mean incorporates the seasonal cycle and any long-term anthropogenic trends for a given variable. We therefore removed the ensemble mean from each simulation to create
30 a time series of anomalies produced solely by internal climate variability. Note that for CO₂ flux, these anomalies represent internal variability in the contemporary air-sea flux of CO₂, or the combined variability of natural and anthropogenic CO₂.



2.3 Climate Indices

Throughout this paper, we regress anomaly time series of variables from each EBUS onto climate indices. Climate index time series were available for each ensemble member for Nino3, the PDO, NAO, Atlantic Multidecadal Oscillation (AMO), and Atlantic Meridional Overturning Circulation (AMOC) through the Climate Variability Diagnostics Package (CVDP; Phillips et al., 2014). We computed the NPGO index for each simulation following Di Lorenzo and Mantua (2016), and these indices are available through the CESM-LENS project page on the NPGO.

2.4 Statistical Analysis and Model Equations

Air-sea CO₂ fluxes in CESM are computed following the parameterization of Wanninkhof (2014):

$$F = k \cdot K_0 \cdot (pCO_2^o - pCO_2^a), \quad (1)$$

where k represents the gas transfer velocity (dependent on the wind speed squared), K_0 the solubility of CO₂ in seawater, and pCO_2^o and pCO_2^a the partial pressures of CO₂ in the surface ocean and atmosphere, respectively.

We use a linear Taylor expansion to quantify the relative contribution of each variable to the overall CO₂ flux anomaly in response to internally generated variability following Lovenduski et al. (2007) and Turi et al. (2014),

$$\Delta F = \frac{\partial F}{\partial U} \Delta U + \frac{\partial F}{\partial pCO_2^{oc}} \Delta pCO_2^{oc}, \quad (2)$$

where $\frac{\partial F}{\partial U}$ and $\frac{\partial F}{\partial pCO_2^{oc}}$ are determined from the model equations and mean values in each EBUS. Δ 's represent the linear regression of the given variable's anomalies onto a climate index. The contributions from ΔpCO_2^{oc} is further decomposed into DIC, Alk, SST, and salinity terms:

$$\Delta pCO_2^{oc} = \frac{\partial pCO_2^{oc}}{\partial DIC} \Delta DIC + \frac{\partial pCO_2^{oc}}{\partial Alk} \Delta Alk + \frac{\partial pCO_2^{oc}}{\partial T} \Delta T + \frac{\partial pCO_2^{oc}}{\partial S} \Delta S. \quad (3)$$

Because DIC and Alk can be diluted by freshwater fluxes, we introduce salinity-normalized DIC (sDIC) and Alk (sAlk),

$$\Delta F = \frac{\partial F}{\partial U} \Delta U + \frac{S}{S_0} \frac{\partial F}{\partial DIC} \Delta sDIC + \frac{S}{S_0} \frac{\partial F}{\partial Alk} \Delta sAlk + \frac{\partial F}{\partial f_w} \Delta f_w + \frac{\partial F}{\partial T} \Delta T + \frac{\partial F}{\partial S} \Delta S. \quad (4)$$

Due to the significance of sDIC anomaly contributions to the total CO₂ flux anomaly in EBUS, we approximate the mechanisms controlling sDIC anomalies following Lovenduski et al. (2007),

$$\frac{d(sDIC')}{dt} = J'_{circ} + J'_{bio} + J'_{ex} \quad (5)$$

where J'_{circ} , J'_{bio} , and J'_{ex} represent the sources and sinks of sDIC' from circulation, biology, and CO₂ flux anomalies integrated over the upper 100m, respectively. See Lovenduski et al. (2007, their Equation 4) for additional details on these terms and their Appendix B for the computation of J'_{bio} in particular.

To compensate for autocorrelation that is characteristic of climate indices and is also introduced from smoothing, we replace the t -statistic sample size N with an effective sample size, N_{eff} :

$$N_{eff} = N \left(\frac{1 - r_1 r_2}{1 + r_1 r_2} \right) \quad (6)$$



where r_1 and r_2 are the lag-1 autocorrelation coefficients of the two time series being correlated (Bretherton et al., 1999; Lovenduski and Gruber, 2005). N_{eff} represents the number of statistically independent measurements.

3 Model Evaluation

CESM-LENS air-sea CO_2 flux climatologies and $p\text{CO}_2$ seasonal cycles were compared to the SOM-FFN (Self-Organizing Map-Feed Forward Network) product from Landschützer et al. (2017) along the four major EBUS outlined by Chavez and Messié (2009). The SOM-FFN is a CO_2 flux product based on numerous observational datasets and is made available at monthly resolution spanning 1982–2015 at $1^\circ \times 1^\circ$ global resolution. Extensive details on and validation of the procedure can be found in Landschützer et al. (2013) and Landschützer et al. (2016).

3.1 CO_2 Flux Climatology

The mean state of Pacific EBUS CO_2 fluxes is particularly well-modeled in CESM-LENS (Figure 1). The CESM-LENS captures the meridional gradient of poleward uptake and equatorward outgassing of CO_2 in the CalCS (Figure 1e). In this and the other EBUS, the coarse resolution model is not capable of resolving the narrow band of nearshore CO_2 outgassing found in high resolution model solutions (e.g., Turi et al., 2014; Fiechter et al., 2014). In the HumCS, the model depicts the strong outgassing that is characteristic of a tropical upwelling system (Figure 1f). The CO_2 flux climatology in the Atlantic systems is more biased in the CESM-LENS. While the SOM-FFN portrays a meridional gradient of relatively weak CO_2 fluxes in the CanCS, the CESM-LENS simulates strong outgassing along the Western Sahara (Figure 1c and g). However, note that the SOM-FFN does not include coastal estimates, which presumably would have stronger outgassing due to coastal and curl-driven upwelling of DIC-enriched waters. Another important caveat is that the data density of $p\text{CO}_2$ in EBUS informing the SOM-FFN is on the order of the Southern Ocean, a notably undersampled region (Figure 2e and f; Bakker et al., 2016). In turn, the EBUS CO_2 fluxes in SOM-FFN are being informed by remote biogeochemical provinces more often than other regions of the ocean (see Landschützer et al., 2014, their Figure 1). The BenCS has the most biased CO_2 flux climatology of the major EBUS in CESM-LENS. Although it simulates the proper meridional gradient, the outgassing cell is nearly 10° too far south and is significantly stronger than in the SOM-FFN (Figure 1d and h).

The BenCS has larger physical biases in CESM-LENS than all other EBUS. Its SST bias is in excess of 7°C with the nominal 1° atmospheric resolution, compared to less than a 1°C bias in the CalCS and CanCS, and a $1\text{--}3^\circ\text{C}$ bias in the HumCS (pers. comm. with RJ Small, 2018). Further, the BenCS only improves to a 5°C bias at 0.5° atmospheric resolution (Gent et al., 2010). This bias is likely driven by the fact that the Angola-Benguela Front is simulated too far south, in addition to deficiencies in upwelling and meridional transport that are caused by unrealistic alongshore wind stress structure (Small et al., 2015). Because these deficiencies are specific to the BenCS, we will only discuss its representation of the $p\text{CO}_2$ seasonal cycle in Section 3.2, and its internal variability in CO_2 fluxes in Section 4.1, but will not perform a full analysis on its connections to larger-scale climate variability.



3.2 $p\text{CO}_2$ Seasonal Cycle

CESM-LENS simulates the $p\text{CO}_2$ seasonal cycle for the EBUS with similar accuracy to its depiction of the mean state – the Pacific systems are generally well-modeled, while larger biases exist in the Atlantic regions. Beginning with the CalCS, CESM-LENS nearly perfectly matches the SOM-FFN in both amplitude and phase (Figure 2a). The system exhibits its maximum $p\text{CO}_2$ (and thus CO_2 outgassing) in August, and its minimum $p\text{CO}_2$ (and thus CO_2 uptake) in April. We further decomposed the model seasonal cycle into its thermal component (driven by the seasonality of SST) and its non-thermal component (driven by the seasonality of factors such as DIC, ALK, and salinity) following Takahashi et al. (2002). This decomposition suggests that the phase of the CalCS seasonal cycle is determined by thermal (solubility) effects, with its amplitude modulated by non-thermal factors (Figure 2a). These non-thermal factors are almost entirely driven by the seasonal cycle of DIC (not shown), which is characterized by photosynthetic uptake of CO_2 in the summer and fall, coinciding with upwelling season. These dynamics are supported by the high-resolution modeling study of Turi et al. (2014), their Figure 9a. In the HumCS, both CESM-LENS and SOM-FFN suggest a dual peak in the seasonal cycle of $p\text{CO}_2$, although the model and observational product slightly disagree in phase and amplitude (Figure 2b). These dual peaks are driven by an interchanging importance between thermal and non-thermal effects. During the austral summer/fall, warm temperatures lead to enhanced $p\text{CO}_2$ that is slightly compensated for by increased biological activity, similar to the singular peak of the CalCS. In the austral winter/spring, intense upwelling of DIC-enriched waters and reduced biological activity that is slightly compensated for by cooler waters leads to a secondary $p\text{CO}_2$ peak (Kämpf and Chapman, 2016). The SOM-FFN suggests that the CanCS behaves similarly to the CalCS, with a single $p\text{CO}_2$ peak in late summer/fall that is in phase with the seasonal cycle of SST (Figure 2c). However, CESM-LENS simulates an extremely damped seasonal cycle for $p\text{CO}_2$ in the CanCS that results from a delicate balance between thermal and non-thermal effects of similar magnitudes. Despite the thermal and non-thermal effects being in the proper phase for a northern hemisphere system, the SST seasonal cycle is too weak and the DIC seasonal cycle too strong in the CanCS in CESM-LENS. Lastly, we find that CESM-LENS simulates the BenCS $p\text{CO}_2$ seasonal cycle nearly 180 degrees out of phase with the SOM-FFN representation (Figure 2d). Similar to the CanCS, the thermal and non-thermal effects are in the proper phase. However, there is a large bias in the magnitude of the DIC seasonal cycle, which overwhelms the thermal seasonality and drives the $p\text{CO}_2$ seasonal cycle entirely out of phase. This bias in the $p\text{CO}_2$ seasonal cycle further illuminates deficiencies in CESM1 in simulating the BenCS. Note that for all the EBUS, the dominance of the thermal effects is likely due to the fact that our area-weighted region encompasses a large domain that is driven by gyre-scale dynamics and downwelling. We would expect non-thermal factors to play an important role in dictating $p\text{CO}_2$ seasonality nearshore in a high-resolution simulation, such as in Turi et al. (2014), their Figure 9b.



4 Results

4.1 Internal Variability in Upwelling Systems

We emphasize the magnitude of internal variability in EBUS CO₂ fluxes in Figure 3 by showing the ensemble mean standard deviation of air-sea CO₂ flux anomalies (ensemble mean subtracted) at each location across the global ocean. Save for the Southern Ocean and subpolar Arctic, the EBUS emerge as regions of high internal variability on a global scale. The HumCS, CanCS, and BenCS in particular have some of the highest internally driven CO₂ fluxes globally. The CalCS has comparatively low internal variability in CO₂ fluxes. The EBUS generally have higher internal variability than other coastal regions and are particularly distinct from the major western boundary currents, which appear to be influenced very little by internal variability (Figure 3). The internal variability can also be isolated as one constituent of the area-weighted CO₂ flux time series for each of the four EBUS, the others being the forced trend and seasonal cycle (Figure 4 (a–d)). The largest absolute internal variability is found in the BenCS and HumCS with values of 0.98 mol m⁻² yr⁻¹ and 1.20 mol m⁻² yr⁻¹, respectively (Table 1). The BenCS is uniquely exposed to variability from the Southern Ocean and Agulhas Current (Reason et al., 2006). The HumCS likely has intense variability due to its proximity to the tropical Pacific Ocean and thus rapid communication with ENSO (e.g., Colas et al., 2008; Montes et al., 2011).

All four systems have statistically significant trends toward a weaker CO₂ source or greater CO₂ sink over 1920–2015 due mainly to the invasion of anthropogenic carbon (Figure 4; Table 1). Note that in the CanCS and BenCS, there is a trend toward more outgassing of natural CO₂, which is compensated for by the relatively large uptake tendency of anthropogenic CO₂ (Table 1). The long-term trend forces the HumCS, CanCS, and BenCS to act as intermittent seasonal sinks by 2015 in some realizations due to the combination of the long-term trend and internal variability (Figure 4). The BenCS and CanCS have the largest uptake of anthropogenic CO₂ over the historical period, although the HumCS has a relatively large uptake of both natural and anthropogenic CO₂ (Table 1). For the HumCS and BenCS, the contemporary CO₂ flux trend is on the order of the magnitude of their seasonal cycles over the course of 96 years. The CanCS is a unique case, where the contemporary trend is more than double the magnitude of its seasonal cycle (Table 1).

The magnitude of internal variability is greater than that of the seasonal cycle for the majority of systems. The non-seasonal component of the total variability (the sum of the seasonal and internal components) is 59% for the HumCS, 73% for the CanCS, and 56% for the BenCS (Table 1). Only the CalCS has a stronger seasonal cycle of CO₂ flux than internal variability, but the non-seasonal component still accounts for 33% of the total variability in this system (Table 1). Perhaps for the CalCS, as well as the other EBUS, more significant internal variability would be captured at a higher resolution that resolves coastal upwelling, such as in Turi et al. (2014, their Figure 8c). Lastly, internal variability in CO₂ fluxes tends to be phase-locked with the seasonal cycle, as the peak magnitudes of internal variability track the ridges and troughs of the seasonal component (Figure 4).



4.2 Climate Variability and CO₂ Fluxes

Our primary goal for each EBUS was to identify the mode of climate variability most strongly associated with its CO₂ flux anomalies. We correlated area-weighted anomalies from the black boxes in Figure 1e–h for each simulation with every grid cell globally for a set of predictor variable anomalies: SST, sea level pressure (SLP), 10m wind speed, and wind stress curl.

5 We then assessed the ensemble mean of the correlations to determine the mode of climate variability associated with the given global spatial pattern. Figure 5 displays one ensemble mean correlation case for the CalCS (a), HumCS (b), and CanCS (c) as well as violin plots showing the spread of correlations across the 34-member ensemble for Pacific (Figure 5d–e) and Atlantic (Figure 5f) modes of variability.

4.2.1 California Current

10 The correlation between CalCS CO₂ flux anomalies and SSTa yields a map suggestive of Pacific Decadal Variability, due to the zonal dipole of correlations in the North Pacific (Figure 5a; Mantua and Hare, 2002; Di Lorenzo et al., 2008). Although similar in structure to the PDO, this map most closely resembles the NPGO (Di Lorenzo et al., 2008). In fact, correlations between the model-based NPGO with annual smoothing and CalCS CO₂ flux yields an r -value of -0.49 ± 0.04 . In comparison, linear correlations with the PDO result in an r -value of 0.24 ± 0.05 (Figure 5d). Thus, we highlight the NPGO as the major mode of
15 climate variability associated with anomalous CO₂ flux in the CalCS.

We find that the CalCS has a single-signed response to the NPGO with anomalous uptake of CO₂ during a positive event, intensifying the mean state of the system as an uptake site (Figure 6). The direct regression of ΔF onto the NPGO results in an anomalous uptake of $0.10 \text{ mol m}^{-2} \text{ yr}^{-1}$ (Table 2), which is roughly 24% of the long-term historical flux mean of $-0.42 \text{ mol m}^{-2} \text{ yr}^{-1}$. The primary contributions to this uptake anomaly come from variations in SST and sDIC, which are
20 mainly driven by changes to offshore gyre dynamics. As the oceanic expression of the North Pacific Oscillation, the NPGO is associated with intensified geostrophic circulation, resulting in increased transport in both the California and Alaskan Coastal Currents (Di Lorenzo et al., 2008). Further, a positive NPGO leads to enhanced upwelling-favorable winds south of Cape Mendocino (Figure S1). During a positive NPGO event, the entire CalCS cools, increasing the CO₂ solubility of the system (Figure 6, Figure S1). Although downwelling is enhanced offshore, increased DIC from the Alaskan Gyre leads to a tendency
25 for outgassing of CO₂ (Figure S1). Nearshore south of Cape Mendocino, increased upwelling of DIC-enriched waters is compensated for by photosynthesis, leading to near-zero CO₂ flux anomalies (Figure S2). North of Cape Mendocino, weakened upwelling and low subsurface DIC anomalies lead to enhanced uptake anomalies (Figures S1, S2). Because the system-wide contributions of SST and sDIC to the anomalous flux nearly balance each other, minor contributions from wind, salinity, sAlk, and freshwater flux push the system in favor of anomalous uptake (Figure 6). The CalCS has the largest relative ensemble
30 spread in sDIC and sAlk (Figure 6; Table 2). This is potentially because of inter-simulation variability in the response of CalCS dynamics to the NPGO due to atmospheric noise (as in the case of ENSO in Deser et al., 2017, 2018) which can directly alter the biogeochemical properties of source waters that feed the region (Pozo Buil and Di Lorenzo, 2017). Although the linear Taylor expansion approximates a CO₂ flux anomaly nearly half that of the direct regression of ΔF onto the NPGO, it is still of



the same sign. This discrepancy is due to the influence of higher-order and cross-derivative terms that we did not account for in our linear approximation.

We also performed this analysis for the CalCS response to a 1σ positive (warm) phase of the PDO (Figure 7a and b). Every ensemble member displayed a dipole response to the PDO (not shown), with anomalous uptake in the nearshore region south of Cape Mendocino, and anomalous outgassing elsewhere in the domain (Figure 7c). This was the only case in which we found a non single-signed response across all ensemble members to any mode of climate variability investigated. However, note that the dipole pattern is quite similar to that of the CalCS response to the NPGO (Figure 6b). Both the nearshore and offshore regions have modest correlations with the PDO, with r -values of -0.16 ± 0.03 and 0.28 ± 0.05 , respectively. The positive phase of the PDO results in anomalously warm SSTs along the CalCS and causes weaker and shallower upwelling cells with higher retention of nutrient- and carbon-depleted surface waters (Figure S3; Chhak and Di Lorenzo, 2007). This aligns with the inverted contributions of SST and sDIC in Figure 7a and b relative to the contributions of these terms in response to the NPGO (Figure 6a). The warming of CalCS SSTs during a positive phase of PDO causes a reduction of CO_2 solubility and thus a tendency toward outgassing (Figure 7). Anomalous poleward coastal winds associated with the positive phase of the PDO result in reduced coastal and curl-driven upwelling along the entire coastline, and weakened curl-driven downwelling offshore (Figure S3). In coordination with reduced subsurface DIC throughout the region, these changes in circulation contribute toward anomalous uptake of CO_2 throughout the CalCS. Note that the nearshore decomposition in Figure 7a has a y -axis range four times smaller than that of the offshore decomposition. This slight uptake anomaly is the result of a delicate balance of minor terms, where the sDIC reduction slightly outweighs the warming effect. On the other hand, the offshore region has contributions from SST and sDIC that are as much as triple the magnitude as that for the NPGO (Table 2). Despite the sDIC reduction being larger than the SST term, the reduced sALK is substantial enough to cause a slight outgassing anomaly offshore (Figure 7b).

The direct response of winds to the NPGO and PDO plays a negligible role in influencing anomalous CO_2 flux in the CalCS (Table 2). Although ΔU in response to the NPGO and PDO is on the order of the HumCS and CanCS, $\frac{\partial F}{\partial U}$ is 3–10 times smaller than the other systems. $\frac{\partial F}{\partial U}$ is based on the climatological mean U , $\Delta p\text{CO}_2$, and Schmidt number. The CalCS has the smallest mean $\Delta p\text{CO}_2$ of the EBUS – just $0.2\mu\text{atm}$. This causes CO_2 flux in the system to be relatively insensitive to fluctuations in the wind.

4.2.2 Humboldt Current

Global correlations between the HumCS CO_2 flux anomalies and SSTa display ENSO as a major influencer, with regions of high correlation focused around the equatorial Pacific. Correlations between HumCS CO_2 flux anomalies and the Nino3 index resulted in an r -value of -0.40 ± 0.04 (Figure 5e). Similar results were found for the Nino3.4 index (-0.38 ± 0.04) and the Nino4 index (-0.36 ± 0.05). We chose the Nino3 index as our primary predictor of HumCS CO_2 flux anomalies, since it is more eastern-focused and thus captures the stronger spatial correlations closest to the HumCS (Figure 5b).

We present the results of a linear Taylor expansion for HumCS CO_2 flux anomalies regressed onto a 1° El Niño in Figure 8 (Eq. 4). We find that the HumCS responds with a nearly single-signed CO_2 uptake anomaly, resulting in a weakening of the climatological outgassing (Figure 8b). Although there is a small region in the northern HumCS that responds with an



outgassing anomaly, it is nowhere near as coherent across the ensemble as was the spatial dipole response of the CalCS to the PDO (Figure 7c). The direct regression of ΔF onto the Nino3 index results in an anomalous uptake of $0.49 \text{ mol m}^{-2} \text{ yr}^{-1}$, which is approximately 18% of the long-term historical mean of $2.8 \text{ mol m}^{-2} \text{ yr}^{-1}$. As in the case of the CalCS, the two major terms contributing to the uptake anomaly are sDIC and SST, which are in opposition to one another (Figure 8a). We would anticipate this to be the case, as an El Niño event induces warming along the HumCS as well as reduces the efficacy of upwelling for bringing carbon- and nutrient-rich waters to the surface due to the presence of an anomalously deep thermocline (Figure S4; Strub et al., 1998). While upwelling-favorable winds tend to decrease along Chile (outside of our study region) during an El Niño event, the coastal wind response along Peru is variable, ranging anywhere from slight downwelling-favorable to slight upwelling-favorable anomalies (Wyrтки, 1975; Enfield, 1981; Huyer et al., 1987).

In CESM-LENS, the HumCS experiences a warming of 0.7°C for a 1^σ El Niño, which results in an outgassing tendency of $0.3 \text{ mol m}^{-2} \text{ yr}^{-1}$ (Table 2). However, sDIC in the system is reduced by 13.2 mmol m^{-3} for the same event, which translates to a large uptake contribution of $0.8 \text{ mol m}^{-2} \text{ yr}^{-1}$ (Table 2). This is an enormous change in sDIC, which is partially driven by the high subsurface DIC bias in the east equatorial Pacific in CESM1 (see Lovenduski et al., 2015, their Figure 2). The large sDIC reduction is due to weakened upwelling and a deepening of the thermocline by advected warm waters from the equatorial Pacific (Figure S4). Although the passage of coastally trapped waves are important in the HumCS, they are not resolved in the coarse resolution CESM-LENS. Lastly, there is a minor outgassing anomaly of $0.06 \text{ mol m}^{-2} \text{ yr}^{-1}$ in response to a slight intensification of wind magnitude during El Niño (Table 2). Despite the significant contributions of wind speed, SST, and sAlk toward outgassing, the large reduction in sDIC drives an uptake anomaly that weakens the HumCS outgassing during an El Niño event. Note that these are the same mechanisms that are responsible for reduced outgassing in the tropical belt in response to an El Niño (Feely et al., 1999).

4.2.3 Canary Current

Correlations between the CanCS CO_2 flux anomalies and SLPa globally reveal a region of high positive r -values just northwest of Africa. This encircles the climatological position of the Azores High, the atmospheric subtropical gyre which forces the CanCS. The climate index that most directly captures variability in the Azores High is the NAO, and will thus be considered the main mode of climate variability that modulates anomalous CO_2 flux in the CanCS. We find modest correlations of 0.28 ± 0.03 between annually smoothed CanCS CO_2 flux anomalies and the NAO (Figure 5f). Relatively lower correlations are expected between anomalous EBUS CO_2 fluxes and atmospheric indices, as the atmosphere is noisier than the more slowly evolving ocean.

Grid cell correlations between CanCS CO_2 flux anomalies and the NAO are displayed in Figure 9b. The CanCS has a nearly single-signed response of increased outgassing during the positive phase of the NAO. The direct regression of ΔF onto a 1σ NAO results in an outgassing anomaly of $0.2 \text{ mol m}^{-2} \text{ yr}^{-1}$ (Table 2), which is 21% of the historical mean of $0.95 \text{ mol m}^{-2} \text{ yr}^{-1}$. Also note that the linear Taylor approximation aligns exactly with the direct regression. As with the other EBUS, the major contributors toward this anomaly are sDIC and SST (Figure 9a). The NAO describes modifications to the intensity of atmospheric gyre circulation between the Azores High and Icelandic Low (Hurrell et al., 2001). During the positive



phase of the NAO, a stronger Azores High leads to intensified alongshore winds and thus more vigorous upwelling (Figure S5). This brings up additional deep cold water which in turn increases the CO₂ solubility of the system, tending toward an uptake anomaly of 0.15 mol m⁻² yr⁻¹ (Table 2). On the other hand, the increased sDIC from intensified upwelling is double the magnitude of the SST contribution, despite the increased biological activity which reduces some of the physical sDIC input, leading to an outgassing anomaly of 0.33 mol m⁻² yr⁻¹. This large sDIC response is driven both by a high $\Delta sDIC$ of 3.9 mmol m⁻³ per 1 σ NAO as well as the fact that the CanCS has the highest $\frac{\partial F}{\partial sDIC}$ of the major EBUS. Increased winds of 0.3 m s⁻¹ per 1 σ NAO lead to a significant outgassing pressure of 0.05 mol m⁻² yr⁻¹. This is due both to a large system sensitivity, $\frac{\partial F}{\partial U}$, to changes in wind and a high wind anomaly in response to the NAO. Ultimately, intensified winds and an anomalous increase in sDIC due to enhanced upwelling counteracts the solubility effects of colder SSTs and increased photosynthetic uptake of sDIC. This leads to the highest relative CO₂ flux anomaly of any system, with a 21% increase in outgassing per 1 σ NAO event relative to the long-term mean.

5 Conclusions and Discussion

We find that the seasonal cycle of pCO_2 is single-peaked and its phase is driven by thermal (solubility) effects in the CalCS, CanCS, and BenCS, while non-thermal effects modulate its amplitude. The seasonal cycle of pCO_2 in the HumCS is dual-peaked and driven by an interchanging importance between thermal and non-thermal factors. Although CESM-LENS models the CalCS and HumCS pCO_2 seasonal cycle well, the CanCS seasonal cycle is damped and the BenCS seasonal cycle entirely out of phase. Variations in sDIC and SST in response to large modes of climate variability exert the most influence on anomalous CO₂ fluxes in the CalCS, CanCS, and HumCS. Further, these terms always act in opposition to one another in the portions of variability associated with the climate indices explored in this study. Secondary to these terms are wind speed and sAlk. Although their contributions do not rival those of SST and sDIC in magnitude, they act to further reinforce anomalies or to tip the balance toward outgassing or uptake when sDIC and SST are of equal magnitude. In all systems, salinity and freshwater fluxes have negligible contributions toward the total CO₂ flux anomaly. CalCS and CanCS CO₂ flux anomalies are associated mainly with climate modes related to the subtropical anticyclonic gyres, with their mean states (uptake for the CalCS and outgassing for the CanCS) intensified during phases of enhanced gyre circulation in the NPGO and NAO, respectively. On the other hand, CO₂ flux anomalies in the HumCS are mostly driven by ENSO, due to its close proximity to the equatorial Pacific. We find that the HumCS has weakened outgassing during El Niño due to reduced upwelling and a deepening of the thermocline, which are similar mechanisms to the equatorial Pacific's response to El Niño (Feely et al., 1999). The major EBUS are often lumped together in studies due to their similarities – they are all characterized by their presence on the eastern flank of subtropical gyres, their Ekman dynamics associated with this positioning which leads to coastal and curl-driven upwelling, their productive fisheries, and in the case of our study, their high variability in CO₂ fluxes. However, we show in this study that their position in terms of latitude and ocean basin as well as their coastal geometry leads to unique physical and biogeochemical responses to climate variability. In particular, despite variations in sDIC being a leading contributor to CO₂ flux anomalies, the drivers of these sDIC anomalies differ between EBUS.



Because sDIC anomalies are so critical to the EBUS response to internal climate variability, we further decomposed these anomalies into their absolute (Table 3) and relative (Figure 10) contributions from circulation (e.g., upwelling, advection, diffusion), biology (photosynthesis, respiration, and calcium carbonate formation and dissolution), and CO₂ fluxes. Changes in biological activity in the HumCS in response to ENSO contribute to nearly 50% (8.611 TgC yr⁻¹) of the total sDIC tendency anomaly (Figure 10, Table 3). During an El Niño (La Niña) enhanced respiration (photosynthesis) pumps sDIC into (out of) the upper water column. While biology is the major contributor to sDIC tendency anomalies in the HumCS, circulation changes play a leading role in the CalCS. In response to the NPGO, circulation anomalies in the CalCS contribute to roughly 47% (1.467 TgC yr⁻¹) of the total sDIC tendency anomaly (Figure 10, Table 3). It is difficult to assess the relative contributions of J'_{circ} and J'_{bio} in the CanCS, as the large ensemble spread in J'_{bio} drives a highly uncertain J'_{circ} , which is computed as the anomaly of the other three terms (Figure 10). In all three systems, CO₂ flux anomalies play an important role in modifying the sDIC tendency, with an ensemble mean relative contribution greater than 25% (Figure 10). Note, however, that significant (moderate) spatial variability exists for circulation and biology contributions in the HumCS (CanCS), while contributions are relatively uniform throughout the CalCS (Figure S7).

It is important to note that anthropogenic climate change will likely modify our findings over the coming decades in a number of ways. The long-term addition of anthropogenic carbon to the surface ocean causes EBUS to become greater sinks for CO₂. This trend shifts the mean state of the EBUS, causing historical outgassing sites (the HumCS, CanCS, and BenCS) to become intermittent net sinks of CO₂ under the influence of internal variability by the end of the historical period (Figure 4). Projecting to 2100 under RCP8.5 forcing, we find that the CanCS and BenCS become net sinks for CO₂ due to the anthropogenic trend, with mean values of -0.43 mol m⁻² yr⁻¹ and -0.04 mol m⁻² yr⁻¹ over 2016–2100, respectively. The addition of anthropogenic CO₂ into the surface ocean can also intensify the magnitude of the seasonal cycle of CO₂ flux. This is due to the increased concentration of CO₂ in the surface ocean as well as the reduction in the ocean's buffer capacity, which makes pCO₂ more sensitive to seasonal fluctuations in DIC and alkalinity (Landschützer et al., 2018, and references therein). This effect has been shown in observations (Landschützer et al., 2018) and is also projected in climate models (Kwiatkowski and Orr, 2018), but is only seen significantly in the CalCS and CanCS, with an approximate 37% and 30% increase in the CO₂ flux seasonal cycle over 2016–2100, respectively. Negligible changes to the seasonal cycle occur in the HumCS and BenCS.

External forcing will also alter the dynamics of the EBUS (Bakun et al., 2015; García-Reyes et al., 2015), potentially inducing changes to alongshore winds (Narayan et al., 2010; Sydeman et al., 2014; Oerder et al., 2015; Rykaczewski et al., 2015; Wang et al., 2015) and upper ocean stratification (Di Lorenzo et al., 2005; Rykaczewski and Dunne, 2010; Oerder et al., 2015), which will in turn influence the rate and efficacy of upwelling. It is unlikely that changes to vertical transport will be detectable until mid-century, as the anthropogenic signal is obscured by internal variability (Brady et al., 2017). However, externally forced trends in stratification are likely to emerge much quicker (Henson et al., 2016). The biogeochemical signature of waters feeding upwelling (e.g., O₂, CO₂, and nutrient concentrations) will likely also be modified due to these dynamical changes as well as to changes to ocean ventilation and source water pathways (Rykaczewski and Dunne, 2010). Externally forced changes in physical and biogeochemical properties of EBUS will likely alter the relative contributions of variables to anomalous CO₂ fluxes, as approximated by Equation 4 and shown in Figures 6–9 and Table 2. It is also possible that modes



of climate variability will change in response to anthropogenic forcing. Model projections and long-term observations have suggested that the intensity, frequency, or variance associated with ENSO (e.g., Timmermann et al., 1999; Cai et al., 2014, 2015), the NAO (Kuzmina et al., 2005), and the NPGO (Sydeman et al., 2013) has changed significantly in recent decades or will change over the next century. While not observed in our historical modeling study, modifications to modes of climate variability associated with the major EBUS could directly influence the magnitude of internally generated anomalies in CO₂ fluxes in the future. Further investigation of the impacts of anthropogenic climate change on CO₂ fluxes in EBUS is necessary for the community.

This study serves as a starting point toward better understanding how internal climate variability modulates CO₂ fluxes in the major EBUS. Here, we only present the leading mode of climate variability associated with anomalous CO₂ fluxes in the HumCS and CanCS, and the leading two modes for the CalCS. Because of this, we explain approximately 16% of the total CO₂ flux variance in the HumCS and 8% in the CanCS. Since we analyzed statistically orthogonal modes (the PDO and NPGO) in the CalCS, we were able to explain as much as 31% of the total CO₂ flux variance. It is difficult to explain a large chunk of the remaining variance for the EBUS, as other modes of internal variability are physically dependent on one another. Further, locally generated atmospheric noise in the EBUS can contribute substantially to the total modeled CO₂ flux variance. Previous studies that relate anomalous CO₂ fluxes to internal climate variability have explained similar amounts of variance. For example, Lovenduski et al. (2007) explains anywhere from 2% to 31% of CO₂ flux variance in the Southern Ocean in response to the Southern Annular Mode (SAM), McKinley et al. (2006) from 6% to 38% in the North Pacific in response to the PDO, and Gruber et al. (2002) 15% in the North Atlantic in response to the NAO.

Our study is limited by our use of a coarse single model ensemble, which carries uncertainty due to structural biases in the representation of the climate system and biogeochemistry, the ensemble's ability to accurately simulate the magnitude and frequency of internal climate variability, and processes that occur at a finer scale than the grid resolution. The community would benefit from future studies involving multiple single-model ensembles, which would reduce uncertainty due to structural biases, such as in the dynamics of the BenCS and the elevated sub-surface DIC concentration in the east equatorial Pacific. Due to model resolution, we do not directly resolve the coastal upwelling process which induces vigorous outgassing within the first O(10km) of the coastline. This problem could be mitigated by nesting high-resolution EBUS simulations within a coarser global ensemble or by using regional mesh refinement techniques. This would allow the remote propagation of climate variability into the EBUS, while avoiding the high computational cost of running multiple high-resolution global simulations. In particular, the BenCS requires significant attention. We find pronounced internal variability in CO₂ fluxes in the BenCS in CESM-LENS that warrants investigation in a high-resolution model specific to the BenCS. We anticipate that these results and further investigation of the relationship between internal climate variability and anomalous CO₂ fluxes in EBUS will be useful for the rapidly developing subseasonal to decadal prediction community. Skillful prediction of climate variability, such as ENSO, the NPGO, and NAO, could be linked directly to anomalous fluxes of CO₂ in the major EBUS. As these systems are naturally sensitive to the undersaturation of calcium carbonate, these predictions could also aid in detecting and managing the onset of seasonal ocean acidification.



Data availability. The output from CESM-LENS is available as single variable time series at monthly, daily, and 6-hourly resolution through the Earth System Grid. Instructions for access and a full listing of available variables can be found under the UCAR Large Ensemble Project web page. Also on the CESM-LENS project page is the Climate Variability Diagnostics Package (CVDP), which includes the climate indices used in this study for every simulation. Instructions for accessing the NPGO index for each simulation as well the code used to generate it can be found at <http://www.cesm.ucar.edu/projects/community-projects/LENS/projects/npgo.html>.

Author contributions. RXB and NSL designed the study. RXB analyzed the data, prepared figures and tables, and wrote the paper. NSL, MAA, MJ, and NG provided invaluable feedback throughout the study and reviewed the paper.

Competing interests. The authors of this study are unaware of any conflict of interest.

Acknowledgements. The National Science Foundation sponsors the National Center for Atmospheric Research where the Community Earth System Model is developed. Computing resources were provided by NCAR's Computational and Information Systems Laboratory. The Department of Energy's Computational Science Graduate Fellowship supported RXB throughout this study (DE-FG02-97ER25308). NSL and RXB are grateful for support from NSF (OCE-1752724, OCE-1558225). NG is grateful for support from the SNF project CALNEX (grant no.149384) and ETH Zürich. We thank A. Phillips for his extensive work on developing the Climate Variability Diagnostics Package. K. Karnauskas, J. Small, and M. Long provided feedback on earlier versions of this manuscript.



References

- D. C. E. Bakker, B. Pfeil, K. M. O'Brien, K. I. Currie, S. D. Jones, C. S. Landa, S. K. Lauvset, N. Metzl, D. R. Munro, S.-I. Nakaoka, A. Olsen, D. Pierrot, S. Saito, K. Smith, C. Sweeney, T. Takahashi, C. Wada, R. Wanninkhof, S. R. Alin, M. Becker, R. G. J. Bellerby, A. V. Borges, J. Boutin, Y. Bozec, E. Burger, W.-J. Cai, R. D. Castle, C. E. Cosca, M. D. DeGrandpre, M. Donnelly, G. Eiseheid, R. A. Feely, T. Gkritzalis, M. González-Dávila, C. Goyet, A. Guillot, N. J. Hardman-Mountford, J. Hauck, M. Hoppema, M. P. Humphreys, C. W. Hunt, J. S. P. Ibáñez, T. Ichikawa, M. Ishii, L. W. Juraneck, V. Kitidis, A. Körtzinger, U. K. Koffi, A. Kozyr, A. Kuwata, N. Lefèvre, C. Lo Monaco, A. Manke, P. Marrec, J. T. Mathis, F. J. Millero, N. Monacci, P. M. S. Monteiro, A. Murata, T. Newberger, Y. Nojiri, I. Nonaka, A. M. Omar, T. Ono, X. A. Padín, G. Rehder, A. Rutgersson, C. L. Sabine, J. Salisbury, J. M. Santana-Casiano, D. Sasano, U. Schuster, R. Sieger, I. Skjelvan, T. Steinhoff, K. Sullivan, S. C. Sutherland, A. Sutton, K. Tadokoro, M. Telszewski, H. Thomas, B. Tilbrook, S. van Heuven, D. Vandemark, D. W. Wallace, and R. Woosley. Surface Ocean CO₂ Atlas (SOCAT) V4, 2016.
- 5 A. Bakun, B. A. Black, S. J. Bograd, M. García-Reyes, A. J. Miller, R. R. Rykaczewski, and W. J. Sydeman. Anticipated effects of climate change on coastal upwelling ecosystems. *Current Climate Change Reports*, 1(2):85–93, Jun 2015. ISSN 2198-6061. <https://doi.org/10.1007/s40641-015-0008-4>.
- R. T. Barber and F. P. Chavez. Biological consequences of El Niño. *Science*, 222(4629):1203–1210, 1983. ISSN 0036-8075. <https://doi.org/10.1126/science.222.4629.1203>.
- 15 R. T. Barber and F. P. Chávez. Ocean variability in relation to living resources during the 1982–83 El Niño. *Nature*, 319:279 EP –, 01 1986.
- A. V. Borges and M. Frankignoulle. Distribution of surface carbon dioxide and air-sea exchange in the upwelling system off the galician coast. *Global Biogeochemical Cycles*, 16(2), 2002.
- M. F. Borges, A. M. P. Santos, N. Crato, H. Mendes, and B. Mota. Sardine regime shifts off Portugal: a time series analysis of catches and wind conditions. *Scientia Marina*, 67(S1):235–244, Apr. 2003. ISSN 1886-8134, 0214-8358. <https://doi.org/10.3989/scimar.2003.67s1235>.
- 20 A. Boyd, J. Salat, and M. Masó. The seasonal intrusion of relatively saline water on the shelf off northern and central Namibia. *South African Journal of Marine Science*, 5(1):107–120, 1987.
- R. X. Brady, M. A. Alexander, N. S. Lovenduski, and R. R. Rykaczewski. Emergent anthropogenic trends in California Current upwelling. *Geophysical Research Letters*, 44(10):5044–5052, 2017.
- 25 C. S. Bretherton, M. Widmann, V. P. Dymnikov, J. M. Wallace, and I. Bladé. The effective number of spatial degrees of freedom of a time-varying field. *Journal of Climate*, 12(7):1990–2009, 1999. [https://doi.org/10.1175/1520-0442\(1999\)012<1990:TENOSD>2.0.CO;2](https://doi.org/10.1175/1520-0442(1999)012<1990:TENOSD>2.0.CO;2).
- W. Cai, S. Borlace, M. Lengaigne, P. Van Rensch, M. Collins, G. Vecchi, A. Timmermann, A. Santoso, M. J. McPhaden, L. Wu, et al. Increasing frequency of extreme El Niño events due to greenhouse warming. *Nature climate change*, 4(2):111, 2014.
- W. Cai, G. Wang, A. Santoso, M. J. McPhaden, L. Wu, F.-F. Jin, A. Timmermann, M. Collins, G. Vecchi, M. Lengaigne, et al. Increased frequency of extreme La Niña events under greenhouse warming. *Nature Climate Change*, 5(2):132–137, 2015.
- 30 W.-J. Cai, M. Dai, and Y. Wang. Air-sea exchange of carbon dioxide in ocean margins: A province-based synthesis. *Geophysical Research Letters*, 33(12), 2006. <https://doi.org/10.1029/2006GL026219>.
- Antonietta Capotondi, Andrew T Wittenberg, Matthew Newman, Emanuele Di Lorenzo, Jin-Yi Yu, Pascale Braconnot, Julia Cole, Boris Dewitte, Benjamin Giese, Eric Guilyardi, et al. Understanding ENSO diversity. *Bulletin of the American Meteorological Society*, 96(6): 921–938, 2015.
- 35 F. Chan, J. A. Barth, C. A. Blanchette, R. H. Byrne, F. Chavez, O. Cheriton, R. A. Feely, G. Friederich, B. Gaylord, T. Gouhier, S. Hacker, T. Hill, G. Hofmann, M. A. McManus, B. A. Menge, K. J. Nielsen, A. Russell, E. Sanford, J. Sevdjian, and L. Wash-



- burn. Persistent spatial structuring of coastal ocean acidification in the California Current System. *Scientific Reports*, 7(1):2526, 2017. <https://doi.org/10.1038/s41598-017-02777-y>.
- F. P. Chavez and M. Messié. A comparison of Eastern Boundary Upwelling Ecosystems. *Progress in Oceanography*, 83(1):80–96, 2009. <https://doi.org/https://doi.org/10.1016/j.pocean.2009.07.032>.
- 5 F. P. Chavez, J. T. Pennington, C. G. Castro, J. P. Ryan, R. P. Michisaki, B. Schlining, P. Walz, K. R. Buck, A. McFadyen, and C. A. Collins. Biological and chemical consequences of the 1997–1998 El Niño in central California waters. *Progress in Oceanography*, 54(1):205–232, 2002. [https://doi.org/https://doi.org/10.1016/S0079-6611\(02\)00050-2](https://doi.org/https://doi.org/10.1016/S0079-6611(02)00050-2).
- FP Chavez, PG Strutton, GE Friederich, RA Feely, GC Feldman, DG Foley, and MJ McPhaden. Biological and chemical response of the equatorial Pacific Ocean to the 1997–98 El Niño. *Science*, 286(5447):2126–2131, 1999.
- 10 D. B. Chelton, P. A. Bernal, and J. A. McGowan. Large-scale interannual physical and biological interaction in the California Current. *Journal of Marine Research*, 40(4):1095–1125, 1982.
- F. Chenillat, P. Rivière, X. Capet, E. Di Lorenzo, and B. Blanke. North Pacific Gyre Oscillation modulates seasonal timing and ecosystem functioning in the California Current upwelling system. *Geophysical Research Letters*, 39(1), 2012. <https://doi.org/10.1029/2011GL049966>.
- 15 K. Chhak and E. Di Lorenzo. Decadal variations in the California Current upwelling cells. *Geophysical Research Letters*, 34(14), 2007. <https://doi.org/10.1029/2007GL030203>.
- F. Colas, X. Capet, J. McWilliams, and A. Shchepetkin. 1997–1998 El Niño off Peru: A numerical study. *Progress in Oceanography*, 79(2–4):138–155, 2008.
- T. E. Cropper, E. Hanna, and G. R. Bigg. Spatial and temporal seasonal trends in coastal upwelling off Northwest Africa, 1981–2012. *Deep Sea Research Part I: Oceanographic Research Papers*, 86:94–111, 2014. <https://doi.org/https://doi.org/10.1016/j.dsr.2014.01.007>.
- 20 M. D. DeGrandpre, T. R. Hammar, and C. D. Wirick. Short-term pCO₂ and O₂ dynamics in California coastal waters. *Deep Sea Research Part II: Topical Studies in Oceanography*, 45(8):1557–1575, 1998. [https://doi.org/https://doi.org/10.1016/S0967-0645\(98\)80006-4](https://doi.org/https://doi.org/10.1016/S0967-0645(98)80006-4).
- C. Deser, I. R. Simpson, K. A. McKinnon, and A. S. Phillips. The Northern Hemisphere extratropical atmospheric circulation response to ENSO: How well do we know it and how do we evaluate models accordingly? *Journal of Climate*, 30(13):5059–5082, 2017.
- 25 C. Deser, I. R. Simpson, A. S. Phillips, and K. A. McKinnon. How well do we know ENSO’s climate impacts over North America, and how do we evaluate models accordingly? *Journal of Climate*, 2018.
- E. Di Lorenzo and N. Mantua. Multi-year persistence of the 2014/15 North Pacific marine heatwave. *Nature Climate Change*, 6(11):1042–1047, 2016.
- E. Di Lorenzo, A. J. Miller, N. Schneider, and J. C. McWilliams. The warming of the California Current System: Dynamics and ecosystem implications. *Journal of Physical Oceanography*, 35(3):336–362, 2005.
- 30 E. Di Lorenzo, N. Schneider, K. M. Cobb, P. J. S. Franks, K. Chhak, A. J. Miller, J. C. McWilliams, S. J. Bograd, H. Arango, E. Curchitser, T. M. Powell, and P. Rivière. North Pacific Gyre Oscillation links ocean climate and ecosystem change. *Geophysical Research Letters*, 35(8), 2008. <https://doi.org/10.1029/2007GL032838>.
- E. Di Lorenzo, J. Fiechter, N. Schneider, A. Bracco, A. J. Miller, P. J. S. Franks, S. J. Bograd, A. M. Moore, A. C. Thomas, W. Crawford, A. Peña, and A. J. Hermann. Nutrient and salinity decadal variations in the central and eastern North Pacific. *Geophysical Research Letters*, 36(14), 2009. <https://doi.org/10.1029/2009GL038261>.
- D. Enfield. Thermally driven wind variability in the planetary boundary layer above Lima, Peru. *Journal of Geophysical Research: Oceans*, 86(C3):2005–2016, 1981.



- R. Escribano, G. Daneri, L. Farías, V. A. Gallardo, H. E. González, D. Gutiérrez, C. B. Lange, C. E. Morales, O. Pizarro, O. Ulloa, and M. Braun. Biological and chemical consequences of the 1997–1998 El Niño in the Chilean coastal upwelling system: a synthesis. *Deep Sea Research Part II: Topical Studies in Oceanography*, 51(20):2389–2411, 2004. <https://doi.org/https://doi.org/10.1016/j.dsr2.2004.08.011>.
- W. Evans, B. Hales, and P. G. Strutton. Seasonal cycle of surface ocean pCO₂ on the Oregon shelf. *Journal of Geophysical Research: Oceans*, 116(C5), 2011. <https://doi.org/10.1029/2010JC006625>.
- 5 RA Feely, T Takahashi, R Wanninkhof, MJ McPhaden, CE Cosca, SC Sutherland, and Mary-Elena Carr. Decadal variability of the air-sea co₂ fluxes in the equatorial pacific ocean. *Journal of Geophysical Research: Oceans*, 111(C8), 2006.
- Richard A Feely, Rik Wanninkhof, Taro Takahashi, and Pieter Tans. Influence of El Niño on the equatorial Pacific contribution to atmospheric CO₂ accumulation. *Nature*, 398(6728):597, 1999.
- 10 Jerome Fiechter, Enrique N Curchitser, Christopher A Edwards, Fei Chai, Nicole L Goebel, and Francisco P Chavez. Air-sea CO₂ fluxes in the California Current: Impacts of model resolution and coastal topography. *Global Biogeochemical Cycles*, 28(4):371–385, 2014.
- G. E. Friederich, P. M. Walz, M. G. Burczynski, and F. P. Chavez. Inorganic carbon in the central California upwelling system during the 1997–1999 El Niño–La Niña event. *Progress in Oceanography*, 54(1):185–203, 2002. [https://doi.org/https://doi.org/10.1016/S0079-6611\(02\)00049-6](https://doi.org/https://doi.org/10.1016/S0079-6611(02)00049-6).
- 15 M. Frischknecht, M. Münnich, and N. Gruber. Remote versus local influence of ENSO on the California Current System. *Journal of Geophysical Research: Oceans*, 120(2):1353–1374, 2015. <https://doi.org/10.1002/2014JC010531>.
- M. Frischknecht, M. Münnich, and N. Gruber. Local atmospheric forcing driving an unexpected California Current System response during the 2015–2016 El Niño. *Geophysical Research Letters*, 44(1):304–311, 2017. <https://doi.org/10.1002/2016GL071316>.
- M. García-Reyes, W. J. Sydeman, D. S. Schoeman, R. R. Rykaczewski, B. A. Black, A. J. Smit, and S. J. Bograd. Under pressure: Climate change, upwelling, and Eastern Boundary Upwelling Ecosystems. *Frontiers in Marine Science*, 2:109, 2015.
- 20 P. R. Gent, S. G. Yeager, R. B. Neale, S. Levis, and D. A. Bailey. Improvements in a half degree atmosphere/land version of the CCSM. *Climate Dynamics*, 34(6):819–833, 2010.
- M. González-Dávila, J. M. Santana-Casiano, and I. R. Ucha. Seasonal variability of fCO₂ in the Angola-Benguela region. *Progress in Oceanography*, 83(1-4):124–133, 2009.
- 25 L. Gregor and P. Monteiro. Is the southern Benguela a significant regional sink of CO₂? *South African Journal of Science*, 109(5-6):01–05, 2013.
- N. Gruber. Carbon at the coastal interface. *Nature; London*, 517(7533):148–149, Jan. 2015. ISSN 00280836.
- N. Gruber, C. D. Keeling, and N. R. Bates. Interannual variability in the North Atlantic Ocean carbon sink. *Science*, 298(5602):2374–2378, 2002. ISSN 0036-8075. <https://doi.org/10.1126/science.1077077>.
- 30 B. Hales, T. Takahashi, and L. Bandstra. Atmospheric CO₂ uptake by a coastal upwelling system. *Global Biogeochemical Cycles*, 19(1), 2005. <https://doi.org/10.1029/2004GB002295>.
- J. Hauck. Unsteady seasons in the sea. *Nature Climate Change*, 8(2):97–98, 2018. <https://doi.org/10.1038/s41558-018-0069-1>.
- C. Hauri, N. Gruber, G.-K. Plattner, S. Alin, R. A. Feely, B. Hales, and P. A. Wheeler. Ocean Acidification in the California Current System. *Oceanography*, 22(4):60–71, Dec. 2009.
- 35 Stephanie A Henson, Claudie Beaulieu, and Richard Lampitt. Observing climate change trends in ocean biogeochemistry: when and where. *Global change biology*, 22(4):1561–1571, 2016.
- James W Hurrell, Yochanan Kushnir, and Martin Visbeck. The North Atlantic Oscillation. *Science*, 291(5504):603–605, 2001.



- James W Hurrell, Marika M Holland, Peter R Gent, Steven Ghan, Jennifer E Kay, Paul J Kushner, J-F Lamarque, William G Large, D Lawrence, Keith Lindsay, et al. The Community Earth System Model: A framework for collaborative research. *Bulletin of the American Meteorological Society*, 94(9):1339–1360, 2013.
- L Hutchings, CD Van der Lingen, LJ Shannon, RJM Crawford, HMS Verheye, CH Bartholomae, AK Van der Plas, D Louw, A Kreiner, M Ostrowski, et al. The Benguela Current: An ecosystem of four components. *Progress in Oceanography*, 83(1-4):15–32, 2009.
- 5 A. Huyer, R. L. Smith, and T. Paluszkiwicz. Coastal upwelling off Peru during normal and El Niño times, 1981–1984. *Journal of Geophysical Research: Oceans*, 92(C13):14297–14307, 1987.
- M. G. Jacox, S. J. Bograd, E. L. Hazen, and J. Fiechter. Sensitivity of the California Current nutrient supply to wind, heat, and remote ocean forcing. *Geophysical Research Letters*, 42(14):5950–5957, 2015.
- 10 Jochen Kämpf and Piers Chapman. *Upwelling Systems of the World*. Springer, 2016.
- J. E. Kay, C. Deser, A. Phillips, A. Mai, C. Hannay, G. Strand, J. M. Arblaster, S. C. Bates, G. Danabasoglu, J. Edwards, M. Holland, P. Kushner, J-F. Lamarque, D. Lawrence, K. Lindsay, A. Middleton, E. Munoz, R. Neale, K. Oleson, L. Polvani, and M. Vertenstein. The Community Earth System Model (CESM) Large Ensemble Project: A community resource for studying climate change in the presence of internal climate variability. *Bulletin of the American Meteorological Society*, 96(8):1333–1349, 2015. [https://doi.org/10.1175/BAMS-D-](https://doi.org/10.1175/BAMS-D-13-00255.1)
- 15 13-00255.1.
- A. W. King, L. Dilling, G. P. Zimmerman, D. M. Fairman, R. A. Houghton, G. Marland, A. Z. Rose, and T. J. Wilbanks. *The first state of the carbon cycle report (SOCCR): The North American carbon budget and implications for the global carbon cycle*. U.S. Climate Change Science Program, Washington, 2007.
- S. I. Kuzmina, L. Bengtsson, O. M. Johannessen, H. Drange, L. P. Bobylev, and M. W. Miles. The North Atlantic Oscillation and greenhouse-gas forcing. *Geophysical Research Letters*, 32(4), 2005.
- 20 L. Kwiatkowski and J. C. Orr. Diverging seasonal extremes for ocean acidification during the twenty-first century. *Nature Climate Change*, 8(2):141–145, 2018. <https://doi.org/10.1038/s41558-017-0054-0>.
- P. Landschützer, N. Gruber, D. C. E. Bakker, U. Schuster, S. Nakaoka, M. R. Payne, T. P. Sasse, and J. Zeng. A neural network-based estimate of the seasonal to inter-annual variability of the Atlantic Ocean carbon sink. *Biogeosciences*, 10(11):7793–7815, Nov. 2013. ISSN 1726-4189. <https://doi.org/10.5194/bg-10-7793-2013>.
- 25 P. Landschützer, N. Gruber, D. C. E. Bakker, and U. Schuster. Recent variability of the global ocean carbon sink. *Global Biogeochemical Cycles*, 28(9):927–949, 2014.
- P. Landschützer, N. Gruber, and D. C. E. Bakker. Decadal variations and trends of the global ocean carbon sink. *Global Biogeochemical Cycles*, 30(10):1396–1417, 2016. ISSN 1944-9224. <https://doi.org/10.1002/2015GB005359>.
- 30 P. Landschützer, N. Gruber, and D. C. E. Bakker. An updated observation-based global monthly gridded sea surface pCO₂ and air-sea CO₂ flux product from 1982 through 2015 and its monthly climatology (ncei accession 0160558). Version 2.2. NOAA National Centers for Environmental Information. Dataset., July 2017.
- P. Landschützer, N. Gruber, D. C. E. Bakker, I. Stemmler, and K. D. Six. Strengthening seasonal marine CO₂ variations due to increasing atmospheric CO₂. *Nature Climate Change*, Jan. 2018. ISSN 1758-678X, 1758-6798. <https://doi.org/10.1038/s41558-017-0057-x>.
- 35 G. G. Laruelle, H. H. Dürr, C. P. Slomp, and A. V. Borges. Evaluation of sinks and sources of CO₂ in the global coastal ocean using a spatially-explicit typology of estuaries and continental shelves. *Geophysical Research Letters*, 37(15), Aug. 2010. ISSN 00948276. <https://doi.org/10.1029/2010GL043691>.



- G. G. Laruelle, R. Lauerwald, B. Pfeil, and P. Regnier. Regionalized global budget of the CO₂ exchange at the air-water interface in continental shelf seas. *Global Biogeochem. Cycles*, 28(11):2014GB004832, Nov. 2014. ISSN 1944-9224. <https://doi.org/10.1002/2014GB004832>.
- G. G. Laruelle, P. Landschützer, N. Gruber, J.-L. Tison, B. Delille, and P. Regnier. Global high-resolution monthly pCO₂ climatology for the coastal ocean derived from neural network interpolation. *Biogeosciences*, 14(19):4545, 2017.
- 5 A. Leinweber, N. Gruber, H. Frenzel, G. E. Friederich, and F. P. Chavez. Diurnal carbon cycling in the surface ocean and lower atmosphere of Santa Monica Bay, California. *Geophysical Research Letters*, 36(8), Apr. 2009. ISSN 0094-8276. <https://doi.org/10.1029/2008GL037018>.
- Keith Lindsay, Gordon B Bonan, Scott C Doney, Forrest M Hoffman, David M Lawrence, Matthew C Long, Natalie M Mahowald, J Keith Moore, James T Randerson, and Peter E Thornton. Preindustrial-control and twentieth-century carbon cycle experiments with the Earth System Model CESM1 (BGC). *Journal of Climate*, 27(24):8981–9005, 2014.
- 10 N. Lovenduski, M. Long, and K. Lindsay. Natural variability in the surface ocean carbonate ion concentration. *Biogeosciences*, 12(21): 6321–6335, 2015.
- N. S. Lovenduski and N. Gruber. Impact of the Southern Annular Mode on Southern Ocean circulation and biology. *Geophys. Res. Lett.*, 32 (11):L11603, June 2005. ISSN 1944-8007. <https://doi.org/10.1029/2005GL022727>.
- N. S. Lovenduski, N. Gruber, S. C. Doney, and I. D. Lima. Enhanced CO₂ outgassing in the Southern Ocean from a positive phase of the Southern Annular Mode. *Global Biogeochem. Cycles*, 21(2), June 2007. ISSN 1944-9224. <https://doi.org/10.1029/2006GB002900>.
- 15 N. S. Lovenduski, G. A. McKinley, A. R. Fay, K. Lindsay, and M. C. Long. Partitioning uncertainty in ocean carbon uptake projections: Internal variability, emission scenario, and model structure. *Global Biogeochemical Cycles*, 30(9):1276–1287, 2016.
- R. Lynn and S. Bograd. Dynamic evolution of the 1997–1999 El Niño–La Niña cycle in the southern California Current System. *Progress in Oceanography*, 54(1-4):59–75, July 2002. ISSN 00796611. [https://doi.org/10.1016/S0079-6611\(02\)00043-5](https://doi.org/10.1016/S0079-6611(02)00043-5).
- 20 N. J. Mantua and S. R. Hare. The Pacific Decadal Oscillation. *Journal of oceanography*, 58(1):35–44, 2002.
- N. J. Mantua, S. R. Hare, Y. Zhang, J. M. Wallace, and R. C. Francis. A Pacific Interdecadal Climate Oscillation with impacts on salmon production. *Bulletin of the American Meteorological Society*, 78(6):1069–1079, June 1997. ISSN 0003-0007. [https://doi.org/10.1175/1520-0477\(1997\)078<1069:APICOW>2.0.CO;2](https://doi.org/10.1175/1520-0477(1997)078<1069:APICOW>2.0.CO;2).
- G. A. McKinley, T. Takahashi, E. Buitenhuis, F. Chai, J. R. Christian, S. C. Doney, M.-S. Jiang, K. Lindsay, J. K. Moore, C. Le Quere, et al.
- 25 North Pacific carbon cycle response to climate variability on seasonal to decadal timescales. *Journal of Geophysical Research: Oceans*, 111(C7), 2006.
- R. Mogollón and P. H. Calil. On the effects of ENSO on ocean biogeochemistry in the Northern Humboldt Current System (NHCS): A modeling study. *Journal of Marine Systems*, 172:137–159, 2017.
- I. Montes, W. Schneider, F. Colas, B. Blanke, and V. Echevin. Subsurface connections in the eastern tropical Pacific during La Niña 1999–
- 30 2001 and El Niño 2002–2003. *Journal of Geophysical Research: Oceans*, 116(C12), 2011.
- J Keith Moore, Keith Lindsay, Scott C Doney, Matthew C Long, and Kazuhiro Misumi. Marine ecosystem dynamics and biogeochemical cycling in the Community Earth System Model [CESM1 (BGC)]: Comparison of the 1990s with the 2090s under the RCP4.5 and RCP8.5 scenarios. *Journal of Climate*, 26(23):9291–9312, 2013.
- N. Narayan, A. Paul, S. Mulitza, and M. Schulz. Trends in coastal upwelling intensity during the late 20th century. *Ocean Science*, 6(3):815,
- 35 2010.
- V. Oerder, F. Colas, V. Echevin, F. Codron, J. Tam, and A. Belmadani. Peru-Chile upwelling dynamics under climate change. *Journal of Geophysical Research: Oceans*, 120(2):1152–1172, 2015.
- Daniel Pauly and Willy Christensen. Primary production required to sustain global fisheries. *Nature*, 374(6519):255–257, 1995.



- Adam S Phillips, Clara Deser, and John Fasullo. Evaluating modes of variability in climate models. *Eos, Transactions American Geophysical Union*, 95(49):453–455, 2014.
- M. Pozo Buil and E. Di Lorenzo. Decadal dynamics and predictability of oxygen and subsurface tracers in the California Current System. *Geophysical Research Letters*, 44(9):4204–4213, 2017.
- 5 C. Reason, P. Florenchie, M. Rouault, and J. Veitch. Influences of large scale climate modes and Agulhas system variability on the BCLME region. In *Large Marine Ecosystems*, volume 14, pages 223–238. Elsevier, 2006. ISBN 978-0-444-52759-2. [https://doi.org/10.1016/S1570-0461\(06\)80015-7](https://doi.org/10.1016/S1570-0461(06)80015-7).
- R. R. Rykaczewski and J. P. Dunne. Enhanced nutrient supply to the California Current Ecosystem with global warming and increased stratification in an Earth System Model. *Geophysical Research Letters*, 37(21), 2010.
- 10 R. R. Rykaczewski, J. P. Dunne, W. J. Sydeman, M. García-Reyes, B. A. Black, and S. J. Bograd. Poleward displacement of coastal upwelling-favorable winds in the ocean’s eastern boundary currents through the 21st century. *Geophysical Research Letters*, 42(15): 6424–6431, 2015.
- J. H. Ryther. Photosynthesis and fish production in the sea. *Science*, 166(3901):72–76, 1969.
- J. M. Santana-Casiano, M. González-Dávila, M.-J. Rueda, O. Llinás, and E.-F. González-Dávila. The interannual variability of oceanic CO₂ parameters in the northeast Atlantic subtropical gyre at the ESTOC site. *Global Biogeochemical Cycles*, 21(1), 2007.
- 15 L. V. Shannon, A. J. Boyd, G. B. Brundrit, and J. Taunton-Clark. On the existence of an El Niño-type phenomenon in the Benguela System. *Journal of Marine Research*, 44(3):495–520, August 1986. <https://doi.org/10.1357/002224086788403105>.
- R. J. Small, E. Curchitser, K. Hedstrom, B. Kauffman, and W. G. Large. The Benguela upwelling system: Quantifying the sensitivity to resolution and coastal wind representation in a global climate model. *Journal of Climate*, 28(23):9409–9432, 2015.
- 20 R Smith, P Jones, B Briegleb, F Bryan, G Danabasoglu, J Dennis, J Dukowicz, C Eden, B Fox-Kemper, P Gent, et al. The Parallel Ocean Program (POP) reference manual ocean component of the Community Climate System Model (CCSM) and Community Earth System Model (CESM). *Rep. LAUR-01853*, 141:1–140, 2010.
- P. T. Strub, J. Mesias, V. Montecino, J. Rutllant, and S. Marchant. Coastal ocean circulation off western South America. In *The Sea*, volume 11. John Wiley, New York, 1998.
- 25 W. Sydeman, M. García-Reyes, D. Schoeman, R. Rykaczewski, S. Thompson, B. Black, and S. Bograd. Climate change and wind intensification in coastal upwelling ecosystems. *Science*, 345(6192):77–80, 2014.
- W. J. Sydeman, J. A. Santora, S. A. Thompson, B. Marinovic, and E. D. Lorenzo. Increasing variance in North Pacific climate relates to unprecedented ecosystem variability off California. *Global Change Biology*, 19(6):1662–1675, 2013.
- T. Takahashi, S. C. Sutherland, R. Wanninkhof, C. Sweeney, R. A. Feely, D. W. Chipman, B. Hales, G. Friederich, F. Chavez, C. Sabine, A. Watson, D. C. E. Bakker, U. Schuster, N. Metzl, H. Yoshikawa-Inoue, M. Ishii, T. Midorikawa, Y. Nojiri, A. Körtzinger, T. Steinhoff, M. Hoppema, J. Olafsson, T. S. Arnarson, B. Tilbrook, T. Johannessen, A. Olsen, R. Bellerby, C. S. Wong, B. Delille, N. R. Bates, and H. J. W. de Baar. Climatological mean and decadal change in surface ocean pCO₂, and net sea–air CO₂ flux over the global oceans. *Deep Sea Research Part II: Topical Studies in Oceanography*, 56(8):554–577, Apr. 2009. ISSN 0967-0645. <https://doi.org/10.1016/j.dsr2.2008.12.009>.
- 30 Taro Takahashi, Stewart C Sutherland, Richard A Feely, and Catherine E Cosca. Decadal variation of the surface water pco₂ in the western and central equatorial pacific. *Science*, 302(5646):852–856, 2003.
- Taro Takahashi, Stewart C. Sutherland, Colm Sweeney, Alain Poisson, Nicolas Metzl, Bronte Tilbrook, Nicolas Bates, Rik Wanninkhof, Richard A. Feely, Christopher Sabine, Jon Olafsson, and Yukihiko Nojiri. Global sea–air CO₂ flux based on climatological surface ocean



- pCO₂, and seasonal biological and temperature effects. *Deep Sea Research Part II: Topical Studies in Oceanography*, 49(9):1601–1622, January 2002. ISSN 0967-0645. [https://doi.org/10.1016/S0967-0645\(02\)00003-6](https://doi.org/10.1016/S0967-0645(02)00003-6).
- D. W. J. Thompson, E. A. Barnes, C. Deser, W. E. Foust, and A. S. Phillips. Quantifying the role of internal climate variability in future climate trends. *Journal of Climate*, 28(16):6443–6456, 2015. <https://doi.org/10.1175/JCLI-D-14-00830.1>.
- 5 A. Timmermann, J. Oberhuber, A. Bacher, M. Esch, M. Latif, and E. Roeckner. Increased El Niño frequency in a climate model forced by future greenhouse warming. *Nature*, 398(6729):694, 1999.
- Rodrigo Torres, David R Turner, José Rutllant, and Nathalie Lefèvre. Continued CO₂ outgassing in an upwelling area off northern Chile during the development phase of El Niño 1997–1998 (July 1997). *Journal of Geophysical Research: Oceans*, 108(C10), 2003.
- G. Turi, Z. Lachkar, and N. Gruber. Spatiotemporal variability and drivers of pCO₂ and air–sea CO₂ fluxes in the California Current System: an eddy-resolving modeling study. *Biogeosciences*, 11(3):671–690, Feb. 2014. ISSN 1726-4189. <https://doi.org/10.5194/bg-11-671-2014>.
- 10 G. Turi, M. A. Alexander, N. S. Lovenduski, A. Capotondi, J. D. Scott, C. A. Stock, J. P. Dunne, J. John, and M. G. Jacox. Response of O₂ and pH to ENSO in the California Current System in a high resolution global climate model. *Ocean Sciences Discussion*, Aug. 2017.
- D. Wang, T. C. Gouhier, B. A. Menge, and A. R. Ganguly. Intensification and spatial homogenization of coastal upwelling under climate change. *Nature*, 518(7539):390, 2015.
- 15 R. Wanninkhof. Relationship between wind speed and gas exchange over the ocean. *Journal of Geophysical Research: Oceans*, 97(C5): 7373–7382, 1992.
- R. Wanninkhof. Relationship between wind speed and gas exchange over the ocean revisited: Gas exchange and wind speed over the ocean. *Limnology and Oceanography: Methods*, 12(6):351–362, June 2014. ISSN 15415856. <https://doi.org/10.4319/lom.2014.12.351>.
- K. Wyrski. El Niño—the dynamic response of the equatorial Pacific Ocean to atmospheric forcing. *Journal of Physical Oceanography*, 5(4):
20 572–584, 1975.

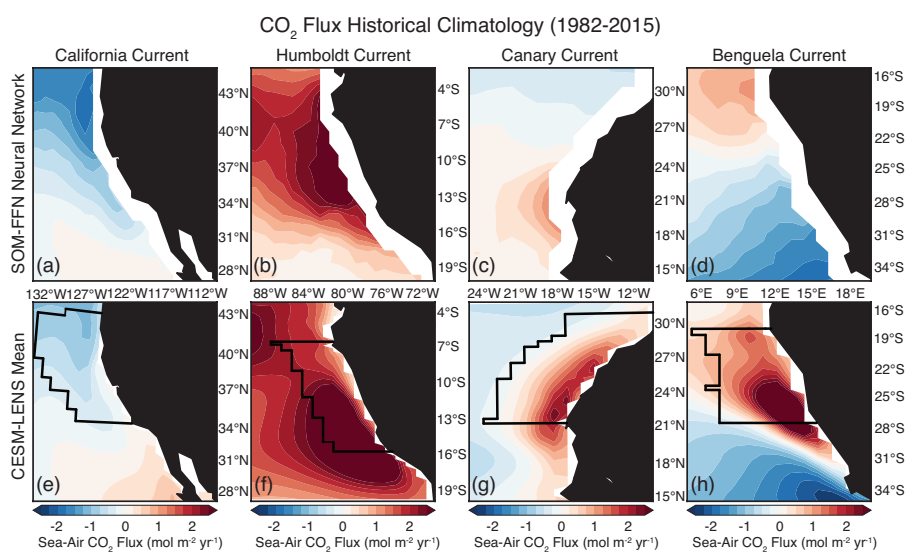


Figure 1. Comparison of CO₂ flux climatology from 1982–2015 between the SOM-FFN (a–d) and the CESM-LENS (e–h). Red denotes outgassing of CO₂ from the ocean to the atmosphere, while blue represents uptake of CO₂ by the ocean. Black lines in e–h follow the model grid and show the region used in each EBUS for statistical analysis, which is based on the 10° latitude of most active upwelling from Chavez and Messié (2009) and confined to 800km offshore.

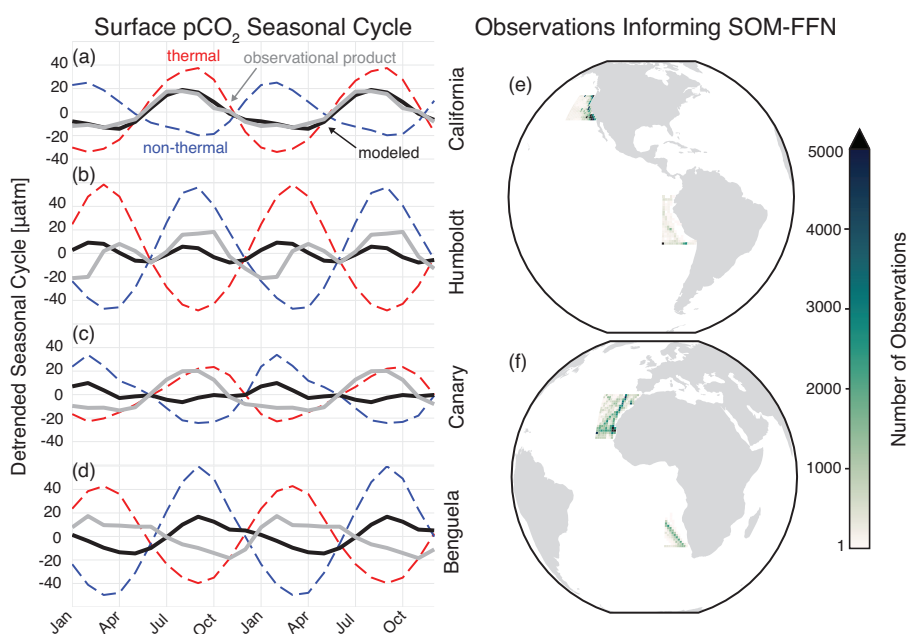


Figure 2. Detrended surface $p\text{CO}_2$ seasonal cycle from 1982–2015 for the SOM-FFN (gray) and the CESM-LENS ensemble mean (black) for the (a) CalCS, (b) HumCS, (c) CanCS, (d) and BenCS. Dashed red lines show the thermal component of the seasonal cycle for the CESM-LENS and dashed blue lines show the non-thermal component. The total number of observations from SOCATv4 contributing to the SOM-FFN for the EBUS is shown in (e) and (f).

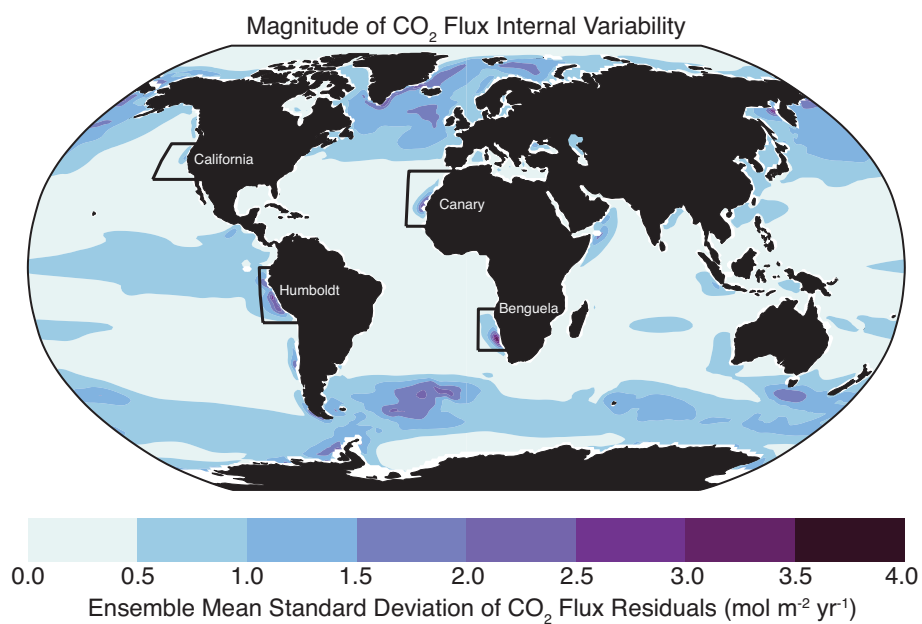


Figure 3. Magnitude of internal variability in CO₂ flux from 1920–2015 in the CESM-LENS. Anomalies were generated by removing the ensemble mean – which represents the seasonality and forced signal – from each realization. Internal variability was then quantified by taking the ensemble mean standard deviation of the anomalies from 1920–2015.

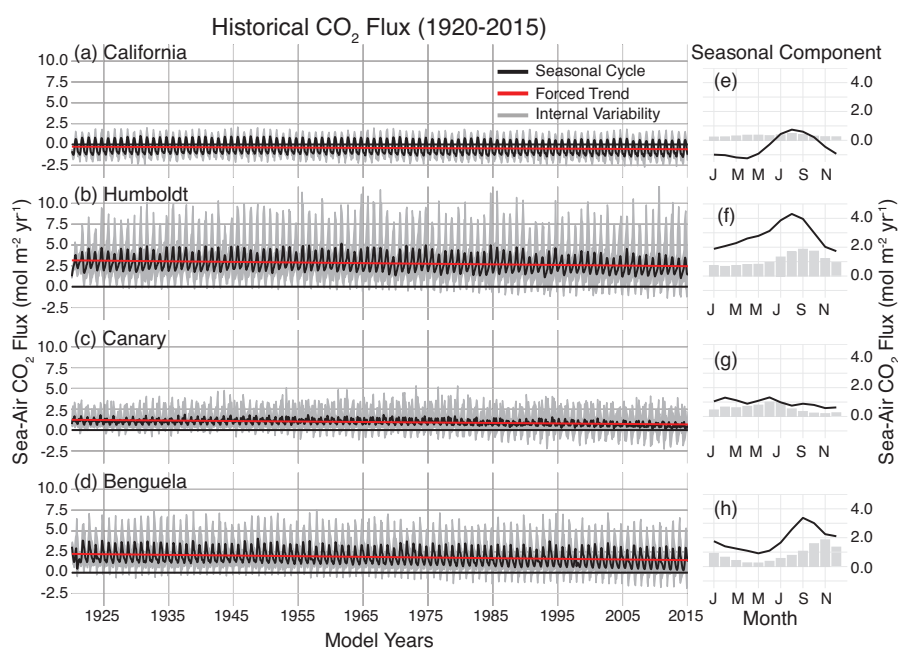


Figure 4. Time series of historical CO₂ flux (1920–2015) in the CESM-LENS for each of the four studied upwelling systems (a–d). The ensemble mean yields both the seasonal cycle (black) and the forced trend (red). Gray shading shows the bounds of the maximum and minimum realizations due to internal variability, but also contains signal from the seasonal cycle and forced trend. Table 1 displays the intercept, seasonality, internal variability, and forced trend for each system. Plots e–h show the mean seasonal cycle (black line) and ensemble mean monthly internal variability (gray bars) for 1920–2015 for each system.

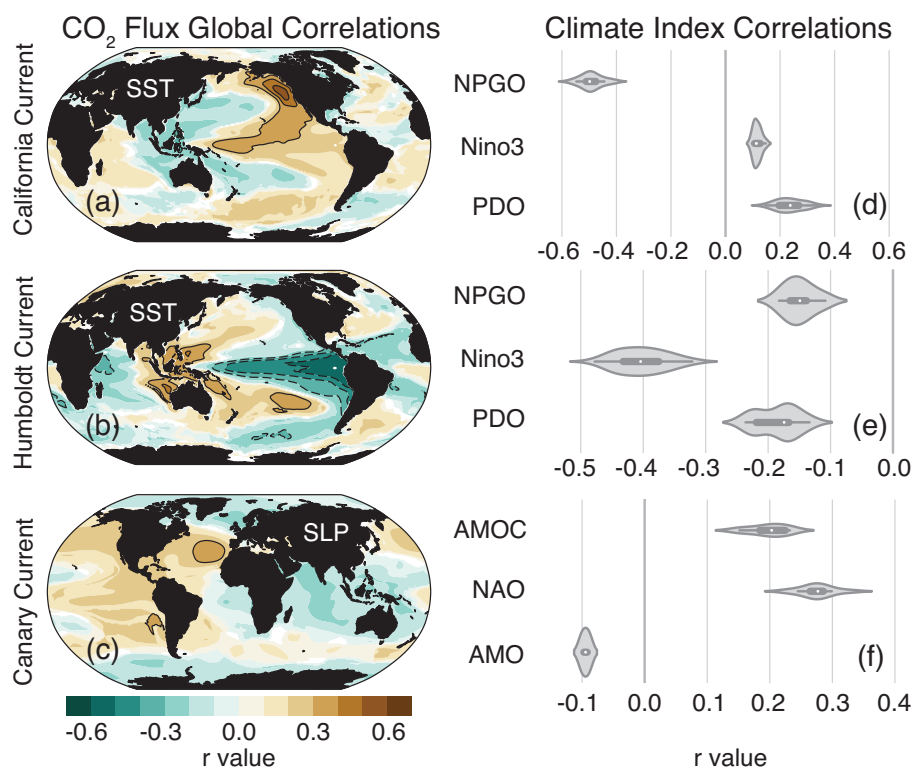


Figure 5. Correlations between area-weighted CO₂ flux anomalies in the statistical study regions outlined in black in Figure 1 (e–g) and SSTa (a–b; California, Humboldt) and SLPa (c; Canary) grid cells globally. Brown colors indicate that positive values of SSTa/SLPa correlate with outgassing, and blue with uptake. Contour lines begin at ± 0.3 and progress in intervals of 0.1. Correlations were performed for each realization individually and the ensemble mean of those global correlations are presented here. Violin plots display correlations between area-weighted CO₂ flux anomalies from (a–c) with major modes of Pacific (d–e) and Atlantic (f) variability.

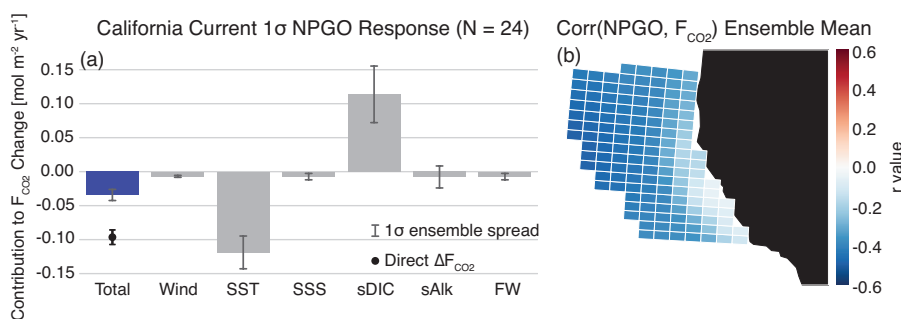


Figure 6. Linear Taylor expansion from Eq. (4) for CalCS CO_2 flux anomalies regressed onto the NPGO (a). Gray bars represent the ensemble mean contributions of each variable to the CO_2 flux anomaly. Error bars represent the one standard deviation spread of the full ensemble. The individual bars sum to the “total” bar to approximate the direct regression of ΔF_{CO_2} onto the NPGO, which is denoted as the black dot with its associated ensemble spread. The ensemble mean grid cell correlations between CO_2 flux anomalies and the NPGO in the CalCS study region are displayed in (b). Positive correlations are associated with outgassing, negative with uptake. Values and ensemble spread for each bar are presented in Table 2.

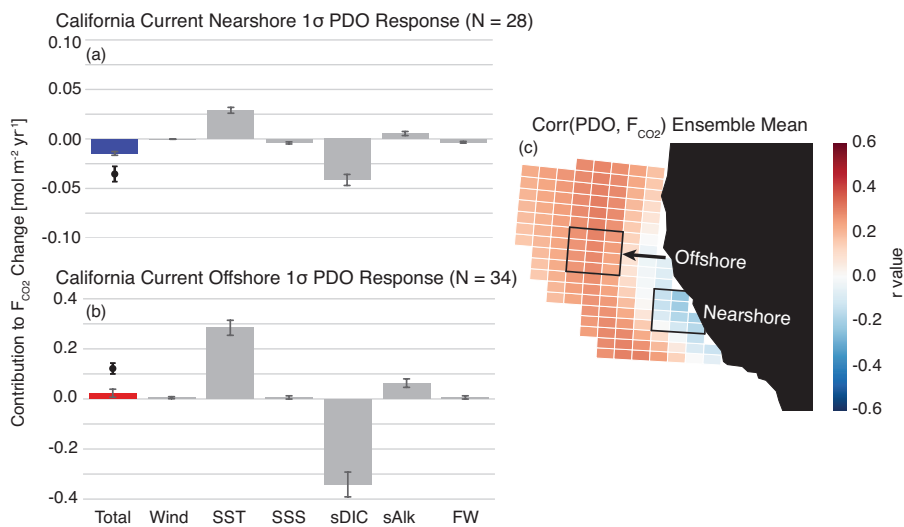


Figure 7. As in Figure 6, but in response to the PDO for a nearshore region (a) and offshore region (b). Note that the offshore decomposition (b) has a y-axis range four times that of the nearshore decomposition (a).

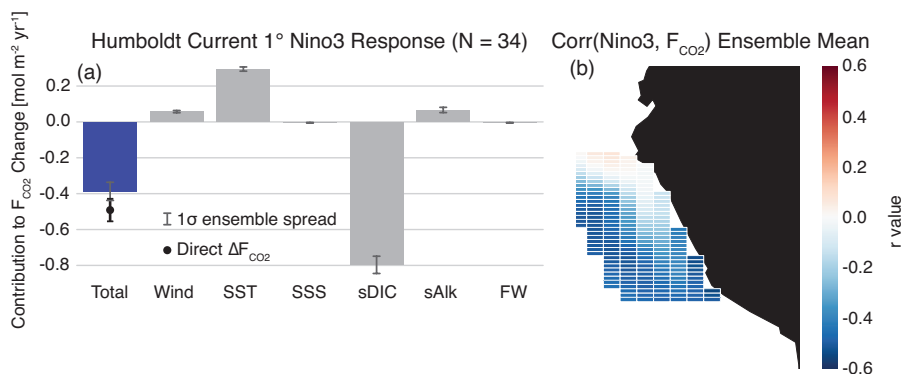


Figure 8. As in Figure 6, but for the Humboldt Current response to the Nino3 index.

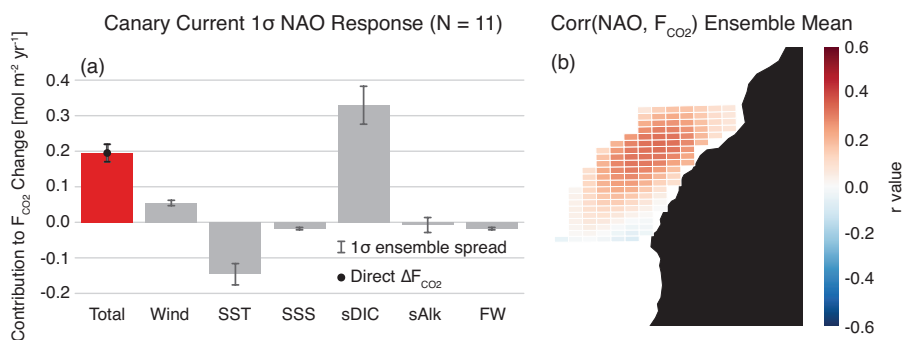


Figure 9. As in Figure 6, but for the Canary Current response to the NAO.

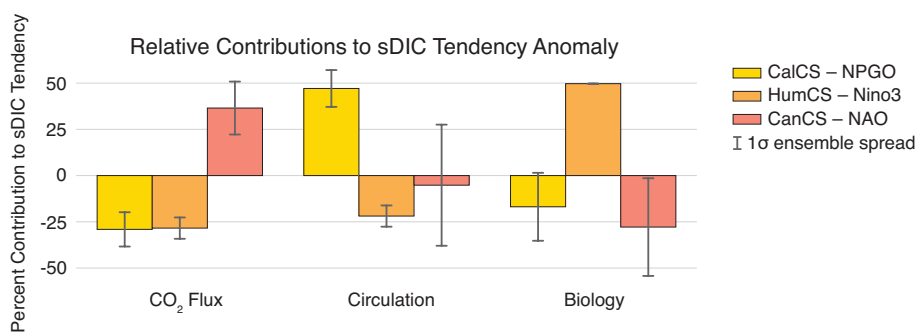


Figure 10. Relative contributions of anomalous CO₂ flux, physical circulation, and biology to the approximated sDIC tendency anomaly for the CalCS (yellow), HumCS (orange), and CanCS (red) in response to the NPGO, Nino3, and NAO, respectively. Error bars show the 1 standard deviation spread of the ensemble. For a given simulation, the absolute values of the three components sum to 100%. These values were approximated using Equation 5.



Table 1. Statistics for CO₂ fluxes in the CalCS, HumCS, CanCS, and BenCS from 1920–2015. The seasonal component is computed as the standard deviation of the ensemble monthly climatology after removing a fourth-order polynomial fit to remove the long-term trend. The internal component is computed as the ensemble mean standard deviation of the anomalies. The trend is computed as the first-order ordinary least squares regression coefficient for the contemporary (total), anthropogenic, and natural CO₂ fluxes. The intercept is derived from this linear regression. The non-seasonal component represents the fraction of total variability (seasonal plus internal) to which the internal component contributes.

Upwelling System	Intercept ¹	Seasonal ¹	Internal ¹	Trend (Contemporary) ²³	Trend (Anthropogenic) ²³	Trend (Natural) ²³	Non-Seasonal Component (%)
California (34° N–44° N)	-0.27	0.71	0.33	-0.31	-0.30	-0.01	31
Humboldt (16° S–6° S)	3.16	0.83	1.20	-0.71	-0.67	-0.04	59
Canary (21° N–31° N)	1.23	0.23	0.62	-0.56	-0.80	0.25	73
Benguela (28° S–18° S)	2.25	0.77	0.98	-0.76	-0.82	0.07	56

¹ mol m⁻² yr⁻¹

² mol m⁻² yr⁻¹ 96yr⁻¹

³ All trends are significant to $\alpha = 0.05$ for a one-sided Mann-Kendall Test

**Table 2.** Estimated contributions to CO₂ flux anomalies, ΔF using Equation 4.

Quantity	CalCS – NPGO	CalCS – PDOo	CalCS – PDO _n	HumCS – Nino3	CanCS – NAO
<i>Individual Terms</i>					
$\frac{\partial F}{\partial U} \Delta U$	-0.01 ± 0.0	0.01 ± 0.0	0.0 ± 0.0	0.06 ± 0.01	0.05 ± 0.01
$\frac{\partial F}{\partial T} \Delta T$	-0.12 ± 0.02	0.28 ± 0.03	0.03 ± 0.0	0.29 ± 0.01	-0.15 ± 0.03
$\frac{\partial F}{\partial S} \Delta S$	-0.01 ± 0.0	0.01 ± 0.01	0.0 ± 0.0	-0.0 ± 0.0	-0.02 ± 0.0
$\frac{S}{S_0} \frac{\partial F}{\partial DIC} \Delta sDIC$	0.11 ± 0.04	-0.34 ± 0.05	-0.04 ± 0.01	-0.8 ± 0.05	0.33 ± 0.05
$\frac{S}{S_0} \frac{\partial F}{\partial Alk} \Delta sAlk$	-0.01 ± 0.02	0.06 ± 0.02	0.01 ± 0.0	0.07 ± 0.01	-0.01 ± 0.02
$\frac{\partial F}{\partial fw} \Delta fw$	-0.01 ± 0.0	0.01 ± 0.01	0.0 ± 0.0	0.0 ± 0.0	-0.02 ± 0.0
<i>Sum of Terms Versus Modeled</i>					
Σ	-0.03 ± 0.01	0.02 ± 0.02	-0.01 ± 0.0	-0.38 ± 0.05	0.21 ± 0.03
ΔF_{mod}	-0.10 ± 0.01	0.12 ± 0.02	-0.04 ± 0.01	-0.49 ± 0.06	0.2 ± 0.02



Table 3. Regression coefficients between the given EBUS and climate index for anomaly time series of the estimated contributions toward the sDIC tendency integrated over the upper 100m and the total surface area of the system, as in Equation 5.¹

Term	CalCS – NPGO	HumCS – Nino3	CanCS – NAO
$\frac{dsDIC'}{dt}$	0.027 ± 0.006	-0.103 ± 0.017	0.044 ± 0.009
J'_{ex}	-0.762 ± 0.195	-4.840 ± 0.613	0.512 ± 0.213
J'_{bio}	-0.677 ± 0.477	8.611 ± 0.813	-0.491 ± 0.543
J'_{circ}	1.467 ± 0.643	-3.873 ± 1.277	0.023 ± 0.552

¹Units are TgC yr⁻¹